**Department of Physics and Astronomy**
**University of Heidelberg**

Bachelor Thesis in Physics
submitted by

**David Schledewitz**

born in Witzenhausen (Germany)

**2021**

# Measurement of the rate and angular distribution of cosmic muons with an ALPIDE telescope

This Bachelor Thesis has been carried out by David Schledewitz at the
GSI Helmholtzzentrum für Schwerionenforschung GmbH, Darmstadt (Germany)
and Physikalisches Institut Universität Heidelberg, Heidelberg (Germany)
under the supervision of
Prof. Dr. Silvia Masciocchi

# Abstract

In preparation for the planned upgrades during the LHC Long Shutdown 2, a new generation of monolithic active pixel sensors (ALPIDE) was developed for the new high-resolution Inner Tracking System of the ALICE detector. These ALPIDE sensors have been rigorously tested and were proven to meet and exceed the requirements for the next LHC runs.

Several tests were performed to investigate the response of the chips, including measurements of cosmic muons. Of particular interest is the ability to detect and track such particles reliably. In this thesis, a seven plane ALPIDE telescope was used to detect cosmic muons and investigate their angular distribution.

First, the identification and analysis of hits are done by comparing the detected muon rate with the theoretical one. Next, a track reconstruction and visualization method is employed, and the quality of the tracks is verified. Consequently, the angular distribution is assessed within the detectable zenith angle range, from 0° to 28°. In the range of more than 4°, the distribution is found to agree rather well with the expected angular distribution of cosmic muons.

Finally, limitations and possible improvements of the experimental setup are discussed to measure the angular distribution with more precision and a wider angular range.

## Zusammenfassung

Im Rahmen des geplanten Upgrades während des LHC Long Shutdown 2 wurde eine neue Generation von Pixeldetektoren (ALPIDE) für das neue hochauflösende Inner Tracking System des ALICE-Detektors entwickelt. Diese ALPIDE-Sensoren wurden intensiv getestet, um zu bestätigen, dass sie die Anforderungen des ALICE-ITS-Upgrades erfüllen.
Es wurden viele Tests durchgeführt, unter anderem Messungen an kosmischen Myonen, um die Antwort der Chips zu untersuchen. Hierbei ist insbesondere, die Fähigkeit solche Teilchen zuverlässig zu erkennen und ihre Spur zu rekonstruieren, interessant. In dieser Arbeit wurde ein ALPIDE-Teleskop mit sieben Sensoren verwendet, um kosmische Myonen zu detektieren und ihre Winkelverteilung zu untersuchen.
Zunächst wurde die Zuverlässigkeit der Messungen sichergestellt, indem die Rate an detektierten Myonen mit der entsprechenden theoretischen Rate verglichen wurde. Als Nächstes wurde eine Methode zur Rekonstruktion und Visualisierung der Spuren eingesetzt, um deren Qualität zu überprüfen. Daraufhin wurde die Winkelverteilung innerhalb des detektierbaren Winkelbereichs (0° - 28°) ausgewertet. Es stellte sich heraus, dass die Winkelverteilung, im Bereich von mehr als 4°, gut mit den Erwartungen für kosmische Myonen übereinstimmt.
Abschließend werden Einschränkungen und mögliche Verbesserungen des experimentellen Aufbaus diskutiert, um die Winkelverteilung präziser und für einen größeren Winkelbereich zu messen.

# Contents

# Chapter 1

# ALICE at the LHC

In the world of science, many interesting open questions exist. Driven by their inquisitiveness, many scientists dedicate their lives to answering those questions, or at least address them. Therefore, many research facilities were founded to focus on different fields of science, like medical science, astronomy, or meteorology, to name only a few. One of these facilities is the *Conseil Européen pour la Recherche Nucléaire*, better known as CERN, near Geneva in Switzerland. It was founded in 1954 and is dedicated to high-energy physics research and aims to answer some of the fundamental scientific issues about our universe [1]. Today CERN's 27 kilometer long *Large Hadron Collider* (LHC) is the world's largest particle accelerator. In September 2008, the first proton beam was injected into the accelerator [2].
Two separate beampipes are built in the LHC in which particles are accelerated in opposite directions, whereby they approach the speed of light. At specific points in the LHC, the resulting particle beams are colliding. At each collision point, an experiment is set and detectors are built to measure the outcome of the collisions. At LHC four main experiments are placed, LHCb [1], ATLAS[2], CMS[3], and ALICE[4]. Next, the ALICE experiment will be discussed in more detail.

## 1.1 ALICE

The main objective of ALICE (*A Large Ion Collider Experiment*) is studying collisions of heavy ions. Even though it was initially the only experiment dedicated to heavy-ion physics, meanwhile all other three main experiments are also studying heavy-ion collisions. Examples for investigated collision systems are lead-lead (Pb-Pb), proton-lead (p-Pb), and proton-proton (p-p).

---

[1] Large Hadron Collider beauty
[2] A Toroidal LHC ApparatuS
[3] Compact Muon Solenoid
[4] A Large Ion Collider Experiment

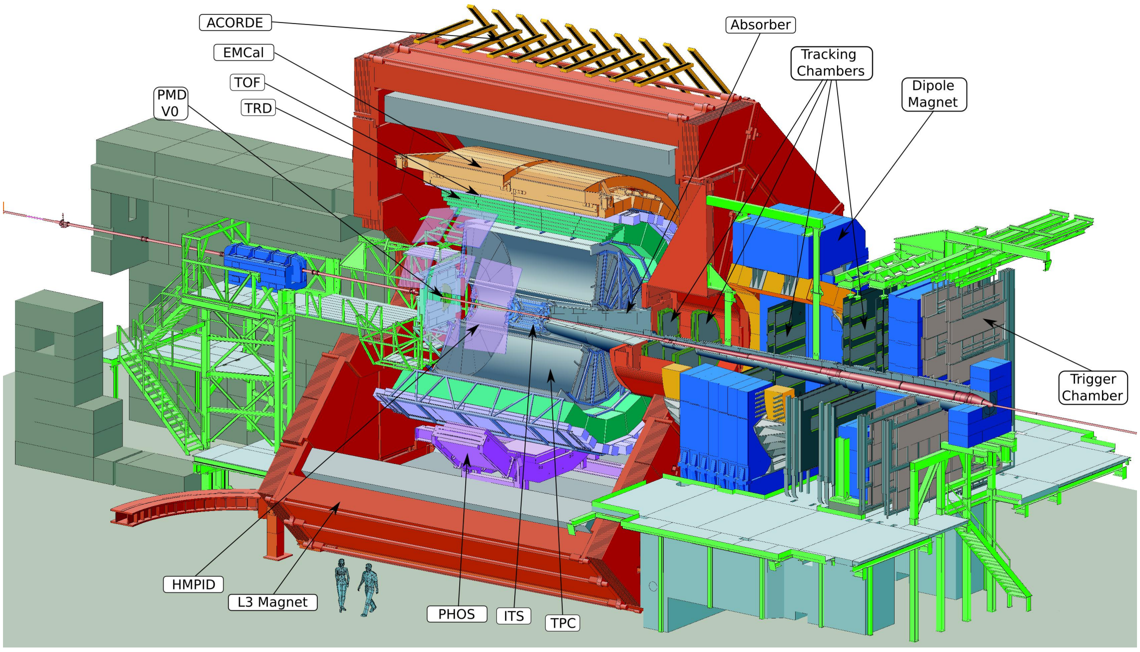

Figure 1.1: Schematic view on the ALICE detector [3]. Abbreviations are explained below or can be found here [4].

To detect the particles produced in these collisions, ALICE uses an advanced detector system with total dimensions of 16 m × 16 m × 26 m and an approximate weight of 10 000 t. The detector is built around the interaction point (IP), where the particle collisions take place. A schematic view on the detector is given in figure 1.1.

The innermost detector, directly surrounding the beampipe, is the *Inner Tracking System* (ITS). It consists of six layers of silicon detectors. The ITS acts as the first part of the tracking system, determining the position of particles traversing the detector with high resolution, thereby identifying the position of primary and secondary vertices of the short-lived particles produced in the collisions. During the *Long Shutdown 2* (LS2), it is replaced by a new generation of pixel detectors as part of the ALICE upgrade. More details to this detector will follow in section 1.2.

In ALICE, the *Time Projection Chamber* (TPC) follows the ITS, which is the central particle tracking system of ALICE. Particles traversing the gas-filled chamber of the TPC ionize the gas, and hence the resulting free electrons drift in the applied electric field of the chamber towards the endcap. There, the arrival time and position of the electrons are measured. With the energy deposited, the trajectory of the initial traversing particle can be reconstructed and allows Particle IDentification (PID).

The *Transition Radiation Detector* (TRD) is the last part of the tracking system of ALICE. The TRD detects the transition radiation of electrons traversing thin layers of radiator materials. Hence, electrons can be discriminated from other charged particles, which also leads to an improvement of PID.

The *Time Of Flight* (TOF) is the next detector layer of ALICE. The TOF consists of Multigap Resistive Plate Chamber (MRPC) layers. Like most of the outer detector layers of ALICE, it functions as an instrument for PID.

The *High Momentum Particle Identification Detector* (HMPID) is a further part of the PID system. It is based on Ring Imaging Cherenkov (RICH) counters. Here the Cherenkov radiation of fast traveling charged particles ($p_T$[5] $>1$ GeV/c) is detected. This detector complements the PID capabilities of TOF for high momentum particles with $p_T > 1$ GeV/c.

The next detector layers are the two electromagnetic calorimeters.

The *PHOton Spectrometer* (PHOS) and the *ElectroMagnetic Calorimeter* (EMCal) aim at measuring the energy of electrons and photons entering them.

Lastly, the *Alice COsmic Ray DEtector* (ACORDE) is used as a trigger for calibration and alignment of ALICE and furthermore for studying high-energy cosmic rays.

A few more detectors are installed in ALICE, like the *Muon Spectrometer* and the *ForWard Detectors* (FWD). Detailed information for these and also the previously mentioned detectors can be found here [4].

To exploit the full potential of the LHC for studying heavy ion collisions, ALICE is upgraded during the LS2 [5]. After the LS2, the LHC increases its luminosity and eventually reaches a Pb-Pb collision rate of up to 50 kHz. The proposed enhancements of the ALICE detector, combined with the significant increase of luminosity provided by the LHC, allow a detailed and quantitative characterization of the high density and high temperature phase of strongly interacting matter, as well as the exploration of new phenomena in this matter. Therefore, high-precision measurements of rare processes at low transverse momenta are required, which can be achieved by enhancing ALICE's low-momentum vertexing and tracking capabilities, as well as increasing extensively the data taking rate.

## 1.2 ITS

The ITS is the innermost detector system of ALICE, with the purpose of tracking and reconstructing of primary and secondary vertices, which are the points, where particles collide or disintegrate. With the energy deposited in the detector, the ITS also contributes to the PID.

---

[5] transverse momentum

To meet the requirements of the ALICE upgrade, amongst other detector systems, a new high-resolution ITS was developed. It provides a very efficient tracking, both in standalone mode and with the TPC, over a wider momentum range with special focus on very low momenta. Furthermore, the vertex reconstruction and the impact parameter, which is the distance of closest approach between a reconstructed track and the corresponding primary vertex and depends on the tracking and vertexing performance, is significantly improved. Another important development is the enhancement of the read-out rate capabilities to exploit the full expected Pb–Pb collision rate.

These enhancements of the ITS are reached by the new highly developed detector technology, the so-called Monolithic Active Pixel Sensor (MAPS). The properties of the detector will be explained in detail in chapter 3.

In the following, the advantages of the new compared to the former ITS are depicted, whereby the references are taken from [6].

**Beampipe** Besides the detector enhancement, also the *beampipe diameter reduction* is an essential part of the upgrade. The beampipe diameter is downsized from 29 mm to 19.2 mm. Due to this reduction, the distance of the first detector layer to the collision point can be lowered.

**Thickness** Not only the beampipe, but also the *thickness of the detector* layers is reduced from 350 µm to 50 µm compared to the previous generation. As a result, the first layer of the ITS upgrade can be placed at an average distance to the collision point (radial position) of 23.4 mm, which is a vast improvement to the 39 mm of the former detector. In combination with the beampipe thickness reduction, this enhancement is particularly important to improve the impact parameter, since the tracking takes place at a closer distance to the collision point. Moreover, the reduced material budget leads to a decreased energy loss of particles traversing the detector layers, which reduces the scattering of low momentum particles.

**Pixel density** Another improvement with direct impact on the tracking precision is the *increased pixel granularity*. Due to the new detector technology, the pixel dimensions of, for example, the first detector layer can be reduced by a factor of 50, from 50 µm × 425 µm down to 20 µm × 20 µm.

**Read-out speed** As already mentioned, one of the key requirements for the ITS upgrade was to *increase* the *read-out rate* from 1 kHz (with close to 100% dead time) of the former ITS to at least 50 kHz to cope with the maximum rate of Pb-Pb collisions achievable after the LS2. With a read-out rate of up to 100 kHz for Pb-Pb collisions, the upgraded ITS even exceeds the requirements by a factor of two.

**Accessibility** One last main upgrade compared to the previous detector generation is the *accessibility* of the ITS during the yearly shutdowns *for maintenance and repair interventions*. Due to this feature, the preservation of high-quality measurements of the ITS can be assured, unlike with the former ITS.

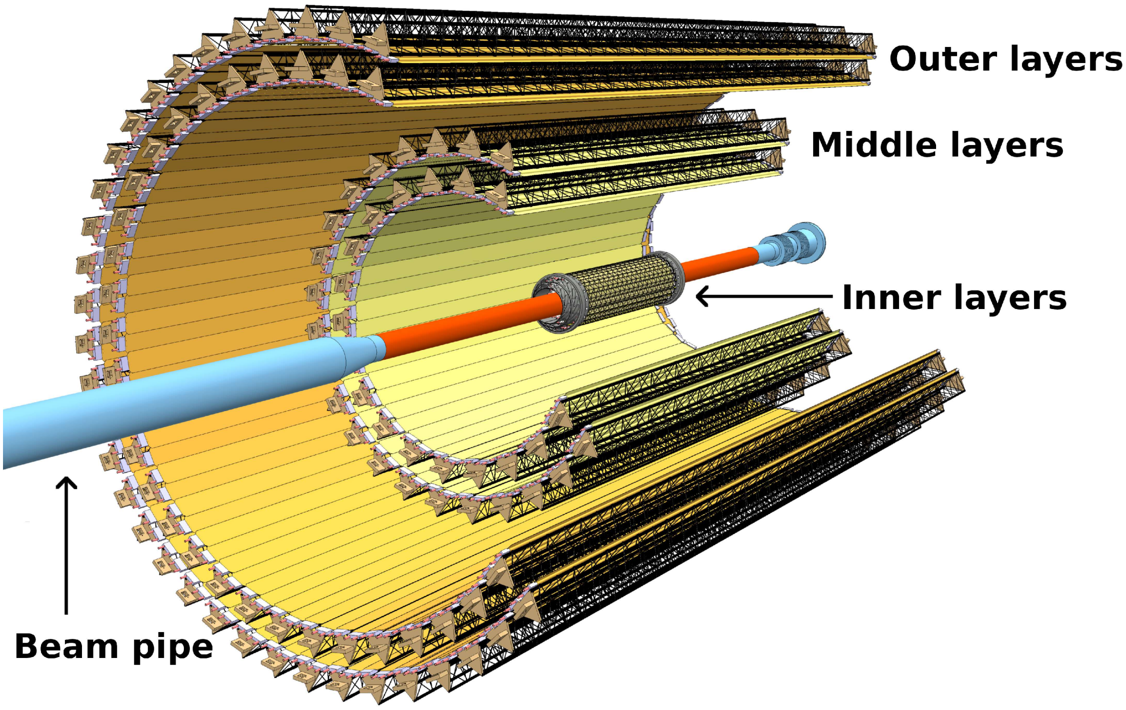

Figure 1.2: Schematic layout of the ITS upgrade [7].

Figure 1.2 depicts the detector layout of the upgraded ITS. The new ITS consists of seven detector layers, which are further separated in an Inner and an Outer Barrel. The three innermost layers are located in the Inner Barrel close to the beampipe. The remaining four layers are located in the Outer Barrel, whereby the Outer Barrel is segmented in two middle and two outer layers. The triangular-shaped structure in each detector layer, shown in figure 1.2, is the so-called Stave, which is an azimuthally segmented detector unit. It includes the supporting structure of the sensors, a cooling system, energy supply, and a hybrid integrated circuit (HIT). The HIT consists of a flexible printed circuit (FPC), which bounds the Pixel Chips and a few passive components. Additionally, each Stave of the Outer Barrel is segmented in two halves, named Half-Stave, each consisting of several modules glued on a cooling unit. The radial positions of the detector layers can be seen in figure 1.3, where a schematic cross-section of the Inner and Outer Barrel is shown.

More details regarding the whole ITS upgrade can also be found here [6, 4].

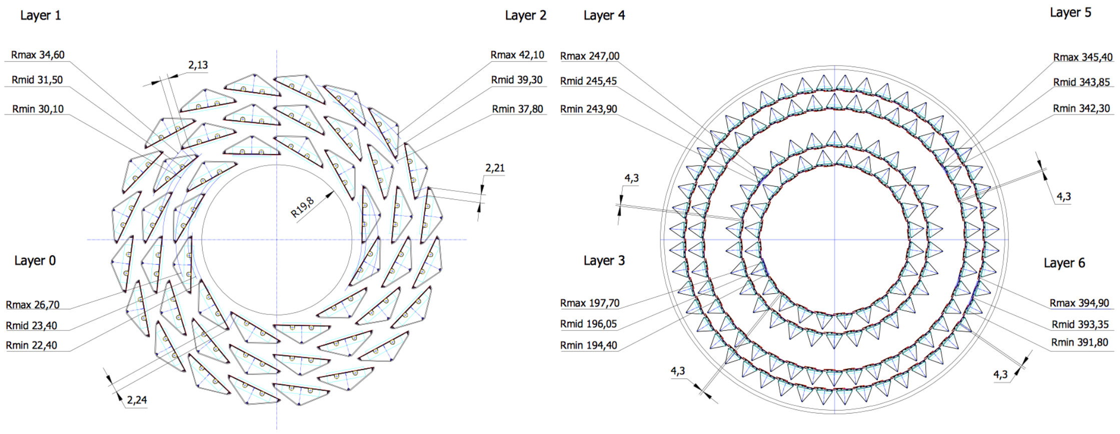

Figure 1.3: Schematic cross-section layout of the ITS upgrade [8]. On the left the Inner Barrel and on the right the Outer Barrel is shown. Minimum, middle and maximum radial positions in mm are indicated for each detector layer.

Before going into the functionality of the MAPS detector, the physics of particle interaction with matter will be introduced in chapter 2, which is crucial to understand how particles and their properties can be measured in the detector.

# Chapter 2

# Particle interactions with matter

## 2.1 Standard model of particle physics

In order to understand the processes of particles interacting with matter and especially with detectors, the basic principles of the Standard Model (SM) of particle physics have to be introduced.
The SM describes the elementary particles that constitute matter and the fundamental forces which mediate their interaction [9]. It consists of twelve fermions, which are particles with spin 1/2, and their corresponding anti-particles. It is completed by four gauge bosons with spin 1, which are the carriers of the fundamental forces, and the spin 0 Higgs boson. A schematic overview of the 17 elementary particles of the SM is given in figure 2.1.
As illustrated, the fermions are further divided into two groups of six particles respectively, called leptons and quarks. In figure 2.1 fermions are sorted in rows with the same properties, like spin and charge, except for their mass. In these subgroups with there is a mass ordering, such that particles with higher mass belong to a higher generation. In contrast to leptons, which exist freely, quarks have to form bound states with other quarks to form so-called hadrons. There are two types of hadrons:

- Mesons: hadrons consisting of a quark and an anti-quark, e.g. $\pi^{\pm}$, $\pi^0$, $K^{\pm}$, $K^0$.
- Baryons: hadrons consisting of three quarks, e.g. $p$, $n$, $\Lambda^0$, $\Delta^0$.

Separating a quark from its bound state requires a high amount of energy. If this energy is applied to a hadron, new quark-antiquark-pairs are created that can form new bound states with the hadron's initial quarks. Most of these hadrons are unstable and decay into stable particles like electrons and protons.
There are four fundamental forces: electromagnetic interaction, weak interaction, strong interaction, and gravity. However, gravity is not included in the SM.

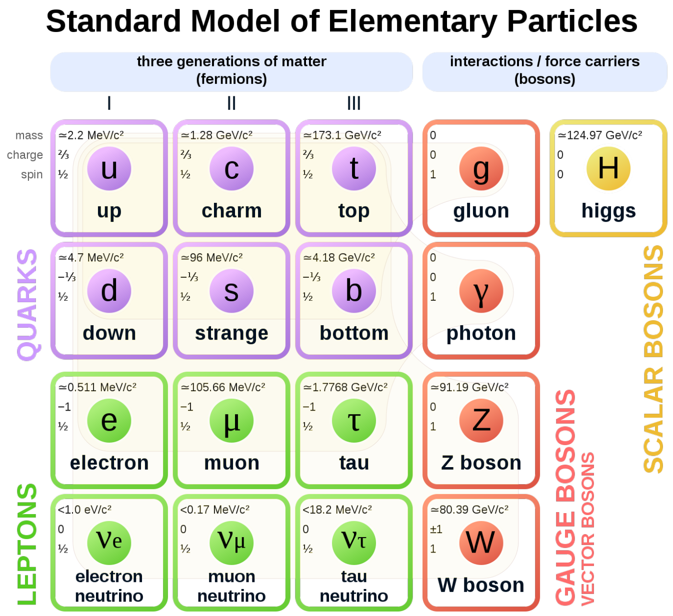

Figure 2.1: Standard model of elementary particles with the 12 fundamental fermions and 5 bosons [10]. The shading indicates which gauge boson interacts with which fermion.

Therefore, the gauge bosons of the SM are mediators for the remaining three fundamental interactions.

The gluon carries color charge and is the mediator of the strong interaction, which couples only to quarks and is responsible for the confinement of quarks in bounded states. The photon is the mediator of the electromagnetic interaction, which couples to all charged fermions. The charged $W^{\pm}$ bosons and the uncharged Z boson are the mediators for the charged- and neutral- current weak interaction, respectively. These bosons couple to all fermions and are the reason for nuclear decay, as well as the interaction of neutrinos with matter [9].

With the knowledge of the fundamental particle interactions the creation of cosmic radiation can be discussed in the following section.

## 2.2 Cosmic radiation

### 2.2.1 Cosmic rays in the atmosphere

Cosmic radiation consists of stable and charged high energy particles, such as electrons, protons, helium, and more rarely heavy nuclei like carbon, oxygen, and iron [11]. Protons are the dominant constituents and make up 90% of the cosmic radiation. All these particles have in common that they were created in stars and accelerated by the explosions of those astrophysical sources. These particles are called *Primary Cosmic Radiation*.

When entering the atmosphere, cosmic rays interact with the air nuclei and produce new particles. These *secondary particles* are still highly energetic and, therefore, interact further with the atmosphere and create more particles. The approximate particle distribution in different regions of the atmosphere is shown in figure 2.2.

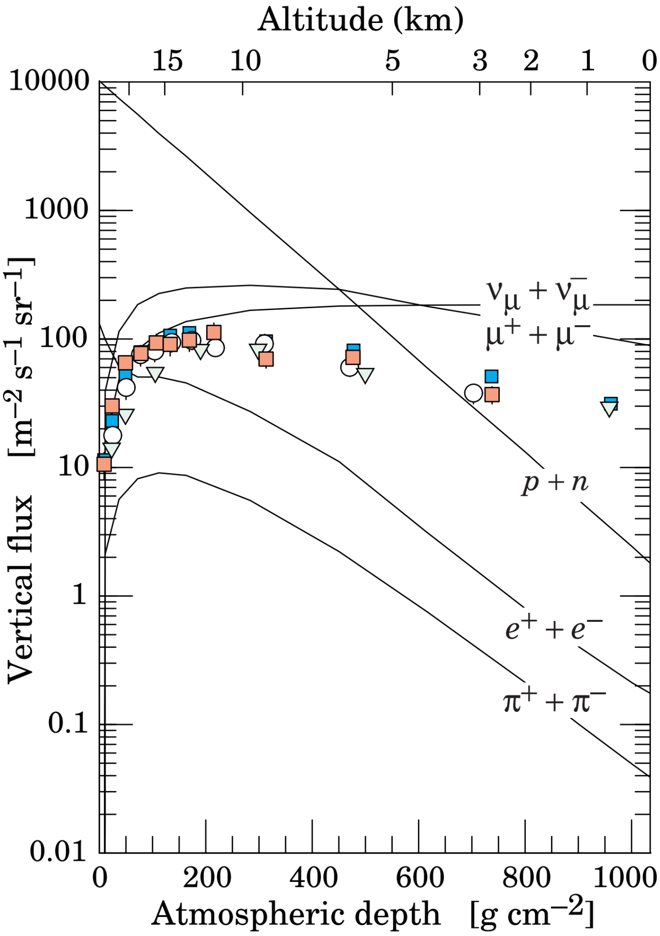

Figure 2.2: Estimated fluxes (perpendicular to the Earth's surface) of cosmic rays in the atmosphere with $E > 1\,\mathrm{GeV}$. The points show measurements of muons with $E_\mu > 1\,\mathrm{GeV}$ [11].

As shown in this figure, the most dominant particles in the top part of the atmosphere are protons and neutrons. In the atmosphere they interact with atmospheric molecules, and mesons are produced. In deeper atmospheric regions muons and neutrinos are the most abundant particles. Those particles are produced in the decay chains of charged mesons like pions and kaons in high atmosphere regions [11]. The most common decays leading to muons are the pion decays by the weak interaction:

$$\pi^+ \rightarrow \mu^+ + \bar{\nu}_\mu \tag{2.1}$$

$$\pi^- \rightarrow \mu^- + \nu_\mu \tag{2.2}$$

### 2.2.2 Muons at sea level

Muons are mostly produced in the high layers of the atmosphere at altitudes of around 15 km. While traversing the atmosphere muons lose around 2 GeV of their energy due to ionization (see section 2.3). This energy loss affects the energy spectrum at sea level for small energies. Besides the energy loss in the atmosphere, the energy and angular distribution of muons is dependent on their production energy spectrum, and their lifetime ($\tau_\mu \approx 2.2 \times 10^{-6}$ s) [11, 12].
Figure 2.3a represents the vertical integral muon momentum spectrum at sea level. This represents the muon flux perpendicular to the Earth's surface at different momenta. The spectrum is nearly flat below 1 GeV/c. The intensity starts to decrease at around 1 GeV/c. At momenta above 100 GeV/c the muon intensity drops even steeper since pions in this energy region tend to interact more with the atmosphere than decaying into muons.

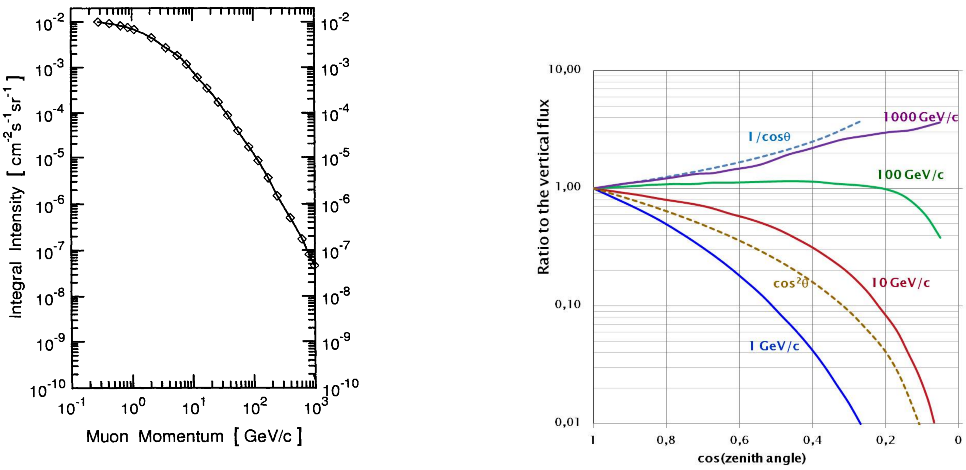

(a) Absolute vertical integral momentum spectrum of muons in the range $0.2 < p_\mu < 1000$ GeV/c at sea level [13]. The veritcal integral intensity of muons is the muon flux perpendicular to the Earth's surface.

(b) Angular distribution of muons at the ground for different muon momenta [14].

Figure 2.3: Momentum and angular distribution of muons at sea level

Next, figure 2.3b shows the angular distribution for muons at sea level with different momenta. The angular distribution varies significantly for different momenta. The distribution is steep at low energies, and the flux decreases with increasing angle. The reason for the decreasing flux at large angles in this energy region is that the muons have to traverse a longer distance through the atmosphere before reaching the ground. Therefore, the energy loss by ionization increases, which increases the minimum energy of a muon to reach the ground. For high energies the distribution is nearly flat or even increases with increasing zenith angle since the muon energy loss does not play a dominant role anymore at high energies. The increasing flux for larger angles at very high energies is caused by pions. As already stated, pions tend to interact with the atmosphere instead of decaying at very high energies. However, at larger angles the distance over which pions can decay and the probability of decaying in the atmosphere increases. As a result, also the muon flux increases. Taking into account that the mean energy for muons at sea level is around $E_\mu \sim 4\,\mathrm{GeV}$, the overall angular distribution is approximately a $\sim \cos^2(\theta)$-distribution, where $\theta$ is the zenith angle [11].

## 2.3 Physics of particle detection

In order to detect particles that are produced in cosmic showers or in high-energy collisions, particle detectors have to be built. High energetic charged particles propagating through matter lose energy mainly by ionization. In this process the particles interact electromagnetically with the atomic electrons of the material through which they pass. Besides ionization, other energy-loss processes can occur, depending on the energy and type of a particle. However, muons lose energy primarily through ionization over a wide momentum range. The Bethe-Bloch formula describes the mean energy loss per unit path length through ionization for all charged particles, but the electron [15].

$$\left\langle -\frac{dE}{dx} \right\rangle = Kz^2 \frac{Z}{A} \frac{1}{\beta^2} \left[ \frac{1}{2} ln \left( \frac{2m_e c^2 \beta^2 \gamma^2 W_{max}}{I^2} \right) - \beta^2 - \frac{\delta(\beta\gamma)}{2} \right] \tag{2.3}$$

z: charge of incident particle
K: constant factor
Z: charge number of traversed medium
A: atomic mass of traversed medium
$m_e$: electron mass
c: speed of light
I: mean excitation energy of traversed medium
$\delta$: density correction of traversed medium
$W_{max}$: maximum energy transfer in a single collision

Here, $\beta = v/c$ represents the relative velocity and $\gamma = \frac{1}{\sqrt{1-\beta^2}}$ the Lorentz factor of the incident particle. $\langle -dE/dx \rangle$ represents the *mass stopping power* with the units

MeV g$^{-1}$ cm$^{2}$. With equation (2.3) the material-density independent stopping power can be determined. The *linear stopping power* is defined as $\rho \langle -dE/dx \rangle$ where $\rho$ is the density of the traversed medium in g cm$^{-2}$. With the exception of density, the rate of ionization energy loss does not depend significantly on the properties of the traversed material. Figure 2.4a shows the mean energy loss through ionization for different materials as a function of $\beta\gamma$ and the muon momentum, respectively.

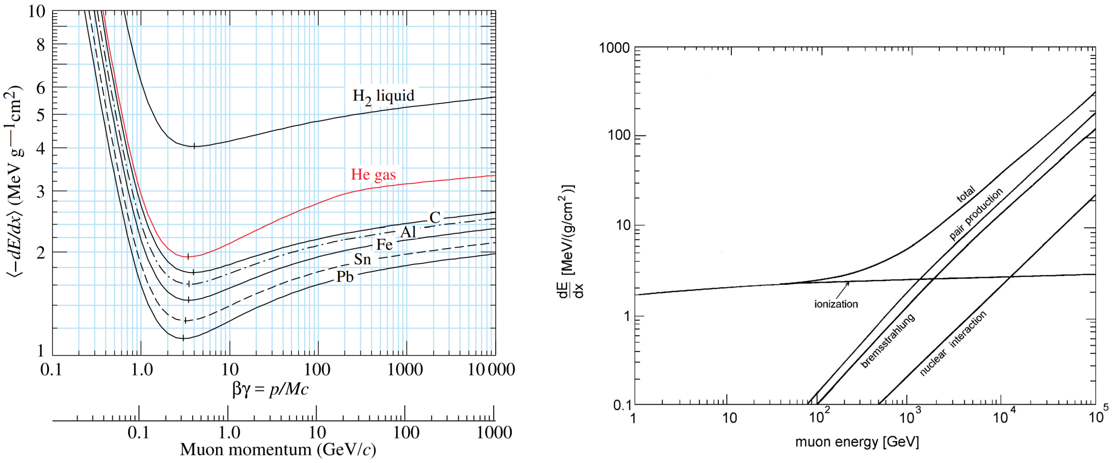

(a) Mean energy loss rate in different materials. Radiative effects are not included [15].

(b) Contributions to the energy loss of muons in rock [16].

Figure 2.4: Mean energy loss rate through ionization and influence of radiative effects.

There are three different regions of the energy loss distribution which are relevant. First, at low momenta around 0.1 to 1 $\beta\gamma$ the energy loss decreases with $\sim 1/\beta^2$ for increasing particle momenta. A broad minimum is reached at a $\beta\gamma$ value of 3 to 4. Particles with a mean energy loss close to this minimum are called *minimum-ionizing-particles* (MIPs). After the minimum the energy loss increases due to the relativistic flattening and extension of the incident particle's electric field. At even higher momenta the electric field polarizes the medium, limiting the field extension and hence damps the relativistic rise of the energy loss.

The Bethe-Bloch formula, as described in equation (2.3), is valid in the region $0.1 \lesssim \beta\gamma \lesssim 1000$. Outside of this region of validity, the Bethe-Bloch formula does not accurately describe the energy loss anymore and corrections have to be considered. At $\beta\gamma \gtrsim 1000$ radiative effects begin to dominate over ionization, as shown in figure 2.4b. These processes are $e^+e^-$ pair production, bremsstrahlung, and photonuclear interaction.

Another limitation for the use of the Bethe-Bloch formula is the thickness of the traversed medium. As mentioned above, the Bethe-Bloch formula describes the mean energy loss through ionization of charged particles traversing matter. However, in thin layers, strong fluctuations from the mean energy loss occur, which are described by the Landau model. This model describes the energy loss probability density function $f(\Delta/x)$, which is also referred to as *energy straggling function*. Here, $\Delta$ is the amount of energy that an incident particle will lose on traversing a layer of thickness $x$.

Figure 2.5a shows the straggling functions for 500 MeV pions in silicon for different layer thicknesses. The figure indicates the most probable energy loss rate and the mean energy loss rate, which is calculated by the Bethe-Bloch formula. For thin layers the most probable and the mean energy loss rate differ significantly. As a consequence, the Bethe-Bloch formula cannot describe the energy loss in thin layers and the Landau model should be used. Figure 2.5b compares the energy loss distribution described by the Bethe-Bloch formula and by the Landau model for different thicknesses of a silicon layer. After the minimum, the energy loss distribution of the straggling functions approaches a plateau, the so-called *Fermi plateau*. Therefore, muons in the energy range of a few GeV to a few hundred GeV have approximately the same energy loss traversing a thin silicon layer [15].

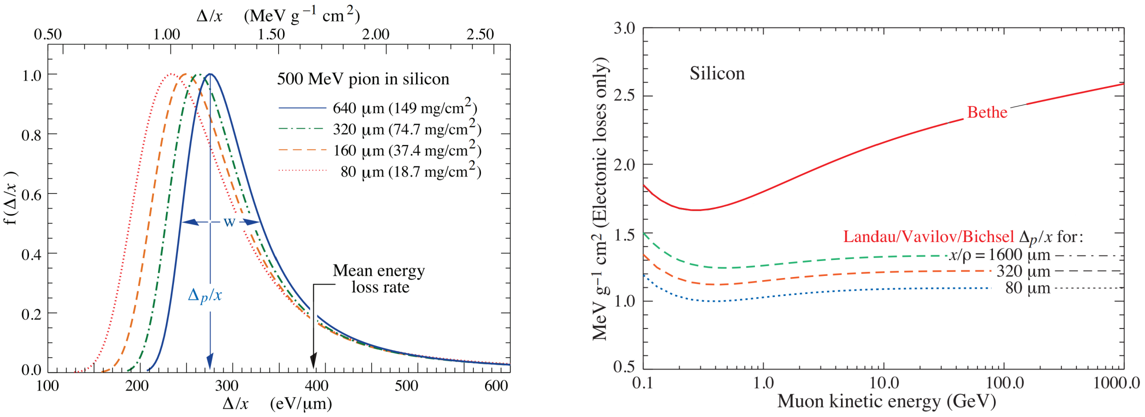

(a) Straggling functions in silicon for 500 MeV pions, normalized to unity at the most probable value $\Delta p/x$. $w$ is the full width at half maximum.

(b) Bethe $dE/dx$ and the Landau most probable energy loss per unit thickness for muons traversing silicon. Radiative losses are excluded.

Figure 2.5: Energy loss fluctuations in thin layers described by the Landau distribution [15].

## 2.4 Semiconductors

### 2.4.1 Properties of intrinsic semiconductors

**Energy band structure** Semiconductors are crystalline materials whose outer shell electrons show an *energy band* structure. The *conduction band* is the energy band with the highest energy. Electrons in this band are detached from their initial lattice atoms, can move freely through the crystal, and as a result cause the conductive behavior of the material. Another band is the *valence band*, which is located at a lower energy level. Electrons in this band are still bound to their lattice atoms. These energy bands can overlap or be separated. In the separated case the region between the energy bands is referred to as *energy gap*. There are no energy levels available for electrons to occupy in the energy gap. As a consequence, an electron in the valence band needs a certain amount of energy to overcome the energy gap and to excited into the conduction band. The energy gap value is determined by material properties. However, it also depends on the temperature and the pressure [17].

Figure 2.6a shows different configurations for the energy band structure. Materials with a large energy gap are called insulators. In insulators at room temperature all electrons are usually in the valence band and cannot be thermally excited into the conduction band. In conductors the energy bands overlap and thus, electrons can easily be excited into the conduction band. In semiconductors an energy gap exists, which is small enough for some electrons to get thermally excited into the conduction band at sufficient temperatures.

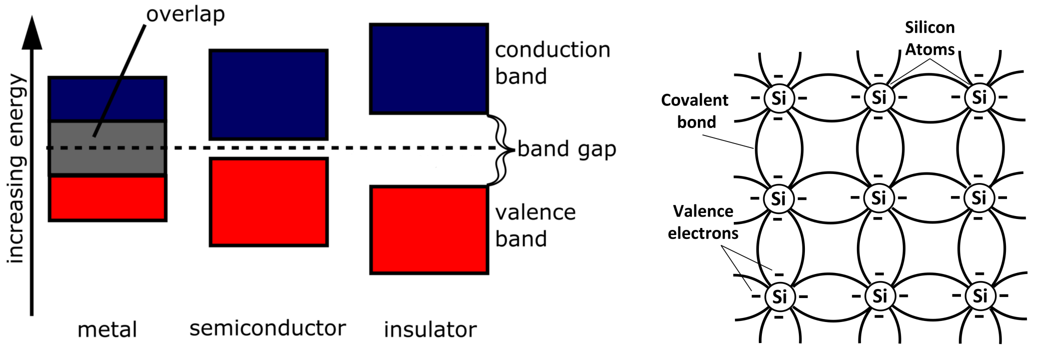

(a) Energy band structure of conductors, insulators, and semiconductors [18].

(b) Covalent bonding in silicon [19].

Figure 2.6: Semiconductor properties

**Charge carriers** At 0 K, a semiconductor's valence band is fully occupied and all electrons participate in the covalent bond between the atoms. Figure 2.6b shows an illustration of the covalent bonding in a pure (intrinsic) silicon semiconductor.

However, at temperatures close to room temperature valence electrons can get thermally excited into the conduction band, leaving a *hole* at their former position in the bonding. A neighboring valence electron can fill this hole, leaving a hole at its original position. As this process continues, the hole appears to move through the lattice. Relative to the negatively charged valence electrons the hole appears as a moving positive charge carrier. Thus, the electric current in semiconductors arises from two sources: the free electrons moving in the conduction band and the holes moving through the valence band.

Besides the creation of new electron-hole pairs, also the recombination of already existing electrons and holes takes place. Therefore, the concentration of electron-hole-pairs reaches an equilibrium under stable environmental conditions. The intrinsic concentration $n_i$ of electrons (or holes) is proportional to:

$$n_i = T^{3/2} \exp\left(\frac{-E_g}{2kT}\right) \tag{2.4}$$

Here, $E_g$ is the energy gap at 0 K, $k$ the Boltzmann constant, and $T$ the temperature [17]. In silicon, the required energy for an electron to be excited into the conduction band is $E_g = 3.6\,\text{eV}$ [20]. At room temperature (300 K) the intrinsic charge carrier concentration is in the order of $n_i \approx 1.5 \times 10^{10}\,\text{m}^{-3}$ [17].

**Mobility** If an electric field is applied to the semiconductor, the electrons and holes drift through the semiconductor with the drift velocity $\nu_e$ and $\nu_h$, respectively. The drift velocities are defined as

$$\begin{aligned} \nu_e &= \mu_e E \\ \nu_h &= \mu_h E \end{aligned} \tag{2.5}$$

where $\mu_e$ and $\mu_h$ represent the *mobilities* of the charge carriers and $E$ the magnitude of the applied electric field. The mobilities are dependent on the material, the temperature, and the electric field for very high electric fields. In silicon, for $E < 10^3\,\text{V}\,\text{cm}^{-1}$ the mobilities are independent from the electric field. At room temperature the mobilities in silicon are $\mu_e = 1350\,\text{cm}^2\,\text{V}^{-1}\,\text{s}^{-1}$ and $\mu_h = 480\,\text{cm}^2\,\text{V}^{-1}\,\text{s}^{-1}$ [17]. With the mobilities, the resistivity of a semiconductor can be determined:

$$\rho = \frac{1}{\sigma} = \frac{1}{e(n\mu_e + p\mu_h)} \tag{2.6}$$

Here, $\sigma$ is the conductivity of the semiconductor, $e$ is the elementary charge, and $n$ and $p$ are the concentrations of free electrons and holes. In the case of intrinsic semiconductors they are equal to the intrinsic charge carrier concentration $n = p = n_i$. The resistivity of intrinsic silicon at 300 K is $\rho \approx 230\,\mathrm{k\Omega\,cm}$ [17].

### 2.4.2 Doped semiconductors

An intrinsic semiconductor has an equal number of free electrons and holes. By adding impurity atoms with a different number of valence electrons, this balance can be changed. In this process, which is referred to as *doping*, the impurity atoms integrate themselves into the intrinsic semiconductor crystal lattice. This new structure is called *doped* or *extrinsic* semiconductor. In a doped semiconductor atoms with an additional valence electron are called *donors* since they provide an additional electron. On the other hand, atoms with fewer valence electrons than the intrinsic material provide an additional hole and are called *acceptors*. The lattice structure and the modified energy band structure of the two types of doped semiconductors are illustrated in figure 2.7.

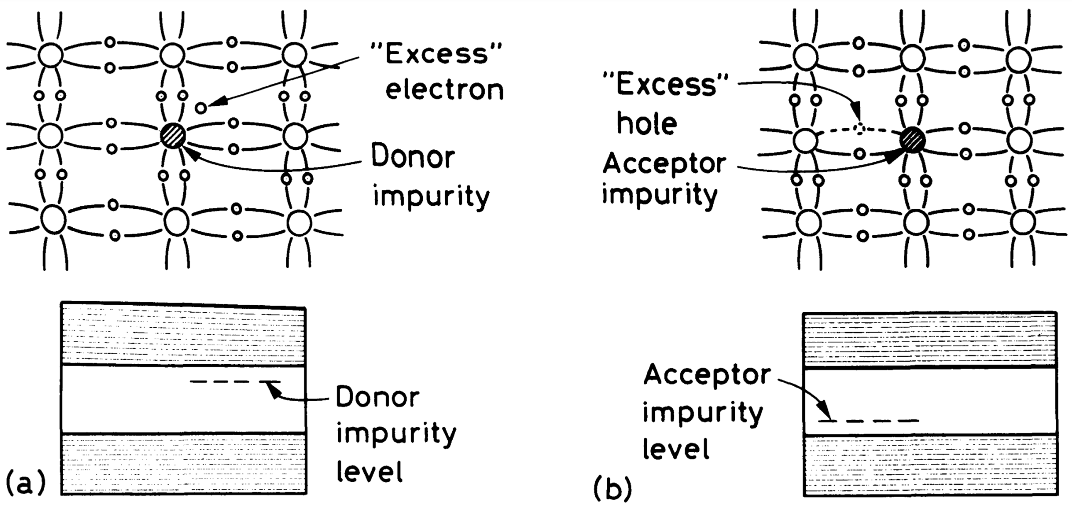

Figure 2.7: (a) Addition of donor impurities. The impurities add excess electrons to the crystal and create donor impurity levels in the energy gap. (b) Addition of acceptor impurities. Acceptor impurities create an excess of holes and impurity levels close to the valence band [17].

In the situation of figure 2.7a the excess electrons can occupy an intermediate discrete energy level created in the energy gap, which is created by the impurity atoms. From this energy level it can more easily excite into the conduction band and thus increase the number of negative charge carriers and the conductivity of the semiconductor. The dominant type of charge carriers in a semiconductor is called the *majority* charge carrier, while the less occurring type is called the *minority*. Such semiconductors, in which electrons are the majority charge carriers, are referred to as *n-type* semiconductors.

In the situation of figure 2.7b the holes are the majority charge carriers and the electrons the minority charge carriers. These materials are called *p-type* semiconductors. The concentration of charge carriers for both types is given by

$$np = n_i^2 = T^3 \exp\left(\frac{-E_g}{kT}\right). \tag{2.7}$$

Since the semiconductor is still neutral, the positive charges have to equal the negative charges in the crystal:

$$N_D + p = N_A + n \tag{2.8}$$

where $N_D$ and $N_A$ represent the donor and acceptor impurity concentrations. In n-type silicon, for example, only donors would be present and thus $N_A = 0$. With $n \gg p$ the negative charge carrier concentration is $n \simeq N_D$. Therefore, the resistivity of an n-type semiconductor would become

$$\rho = \frac{1}{eN_D\mu_e}. \tag{2.9}$$

The calculations for a p-type semiconductor can be performed analogously [17].

### 2.4.3 The pn-junction

An elementary part of building semiconductor detectors and electronic devices is the formation of a junction between an n-type and a p-type semiconductor. The difference in the concentration of electrons and holes between the two differently doped materials causes an initial diffusion of electrons into the p-doped region and holes into the n-doped region. As a consequence, the diffused electrons and holes recombine with the corresponding majority charge carriers and lead to a potential difference between the two regions. The p-type region becomes negatively charged and the n-type region becomes positively charged. The now charged regions create an electric field gradient, which stops the diffusion process, leading to an equilibrium state. In this state the contact region of the material is depleted of charge carriers and is therefore called *depletion region* or *space charge region*. If electrons or holes are created in the depletion region, they will be accelerated out of this region by the electric field.

Figure 2.8 illustrates the pn-junction with a depletion region. The figure also depicts the idealized distribution of the charge density, the electric field, and the potential. The width of the depletion region can be calculated with the Poisson equation

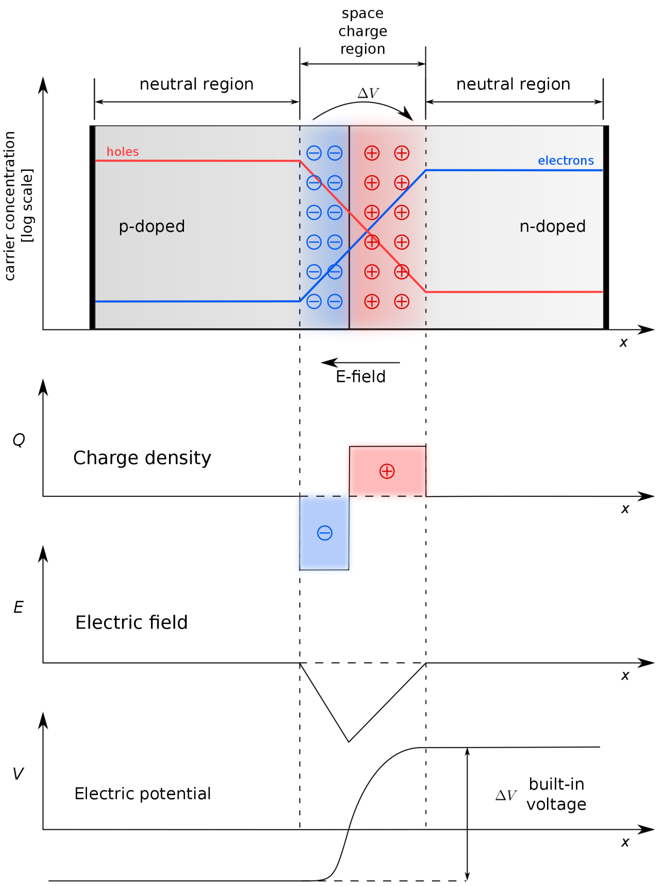

Figure 2.8: A pn-junction in thermal equilibrium. Distributions of the charge density, the electric field, and the potential difference are plotted [21].

$$\frac{d^2V}{dx^2} = -\frac{\rho(x)}{\epsilon} \tag{2.10}$$

where $\epsilon$ is the dielectric constant and the idealized charge density distribution is

$$\rho(x) = \begin{cases} eN_D & -x_n < x < 0 \\ -eN_A & 0 < x < x_p \end{cases} \tag{2.11}$$

Here, $e$ is the electron charge, and $x_n$ and $x_p$ are the depths of the depletion region in the n-doped and p-doped side, respectively. The calculated depletion depth $d$ is

$$d = x_n + x_p = \sqrt{\frac{2\epsilon}{e} \frac{N_D + N_A}{N_D N_A} \Delta V} \tag{2.12}$$

where $\Delta V$ represents the built-in voltage (compare figure 2.8). The whole calculation is detailed in [17]. Using equation 2.9, it can be shown that the depletion depth $d$ (equation 2.12) is related to the resistivity $\rho$ in the following way:

$$d \sim \sqrt{\rho \cdot \Delta V} \tag{2.13}$$

For particle detection purposes, the depletion region should be as large as possible since particles produce a signal mainly in this region. Therefore, high impedance silicon is preferred for the detector design, as it leads to an increased depletion depth (see equation 2.13). According to equation 2.13, another opportunity to enlarge the depletion region is to increase the potential difference in the pn-junction. In order to achieve this, a *reverse-bias voltage* can be applied to the junction by connecting a negative voltage to the p-region and a positive voltage to the n-region. This voltage will attract the majority charge carriers on each side from the junction to the margin of the material. In this process the depletion region is increased by

$$d = \sqrt{\frac{2\epsilon}{e} \frac{N_D + N_A}{N_D N_A} (\Delta V + V)} \tag{2.14}$$

where V is the applied reverse bias voltage. Equation 2.13 can be extended in the same way:

$$d \sim \sqrt{\rho \cdot (\Delta V + V)} \tag{2.15}$$

With the reverse-voltage applied to the junction, the width of the depletion region can be extended up to a few mm. Apart from the larger depletion region, also the charge collection efficiency is increased due to the stronger electric field [17].

# Chapter 3

# The ALice PIxel DEtector (ALPIDE)

In this chapter the *ALice PIxel DEtector* (ALPIDE) is discussed. This detector is developed and designed for the ALICE ITS upgrade (see section 1.2) and is used within the scope of this thesis.

## 3.1 Principle of MAPS

**MAPS and hybrid sensors** Semiconductor sensors are often used in particle physics experiments as part of the particle tracking systems, including the LHC experiments ATLAS, CMS, LHCb, and ALICE. Compared to other tracking detector systems, e.g., gas detectors, some advantages of semiconductor detectors are the small utilized space, the read-out speed, and a high spatial resolution [20, 22].

Typically *hybrid pixel detectors* are used, where the silicon sensor layer is bump-bonded to the read-out electronics, which process the signal (see figure 3.1). With this structure a large depletion region can be produced in the sensor layer. Therefore, a high amount of electron-hole pairs can be produced and collected, leading to a greater signal amplitude.

This technology also has restrictions in terms of material thickness, costs, and pixel size, which limit the spatial resolution of the detector. In order to overcome these limitations, a new sensor technology was developed, where the read-out electronics and the sensor are merged into one single silicon layer. One model of this detector type is shown in figure 3.2a and is referred to as *Monolithic Active Pixel Sensor* (MAPS). Here, monolithic means that the read-out electronics and the sensor are on the same substrate. Active means that at least one amplifier is included in the in-pixel electronics. The MAPS still has disadvantages. The reduced material thickness leads to a smaller signal compared to the hybrid sensor due to less charge collection.

However, this detector technology meets the requirements of heavy-ion experiments and is therefore used for the newest generation of the inner tracking system of ALICE (see section 1.2) [20, 6].

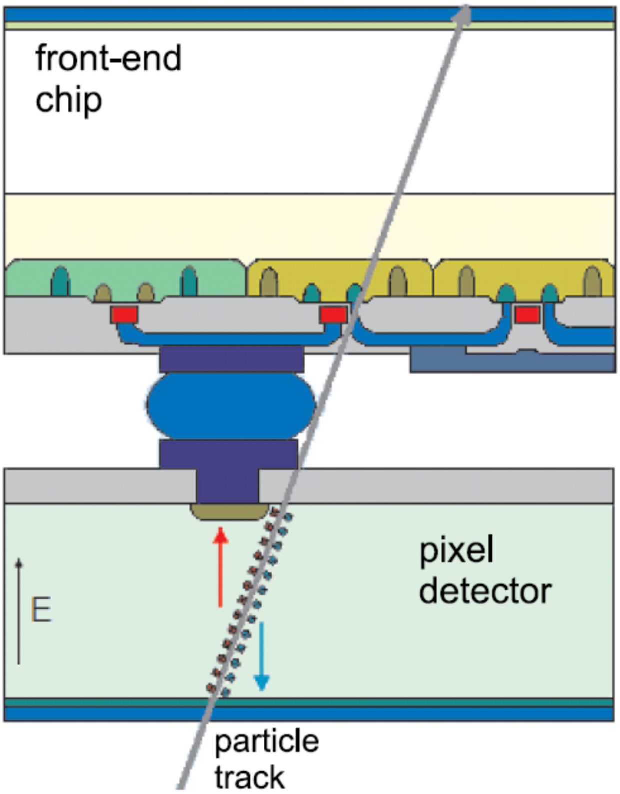

Figure 3.1: Transverse section of a hybrid pixel. The pixel consists of a Si-sensor (bottom layer) bump-bonded to read-out electronics (upper layer). The grey line indicates a particle track [20].

**Signal detection** One type of MAPS detectors, the ALPIDE, consists of three main layers. These layers are depicted in the transverse section of a pixel cell in figure 3.2a. The bottom layer is a highly p-doped substrate ($p^{++1}$), which acts as a reflective barrier for electrons in the middle layer due to the built-in voltage (see section 2.4.3). This middle layer consists of a $p^{-}$-doped[2] material and is referred to as *epitaxial* layer. In this layer the main charge production and collection takes place. On top of the epitaxial layer n-type and p-type implants are located, which are referred to as *n-wells* and *p-wells*. N-wells which are directly connected to the epitaxial layer act as charge collecting diodes. Only in the close environment of the collection diodes the epitaxial layer is depleted (see the white region in figure 3.2a).

---

[1] A $p^{+}$-doped material has a significantly higher concentration of dopants than a p-doped material. The same is valid for $p^{++}$-doped compared to $p^{+}$-doped materials.

[2] A $p^{-}$-doped material has a significantly lower concentration of dopants than a p-doped material.

To increase the depleted region, a small voltage[3] is applied to the collection diode. The depletion region can be further increased by applying an additional reverse bias voltage[4] $V_{BB}$ (also called back-bias voltage). The p-wells are hosting the circuitry of the pixel sensor and prevent the electrons from the epitaxial layer from entering and interfering with the circuitry. Moreover, some MAPS detectors, like ALPIDE, provide a complex in-pixel circuitry by implementing PMOS[5] transistors. They can only operate on n-wells, which have to be isolated from the epitaxial layer to prevent charge collection by the n-well. The separation is achieved by an additional p-well layer, referred to as deep p-well [20, 23].

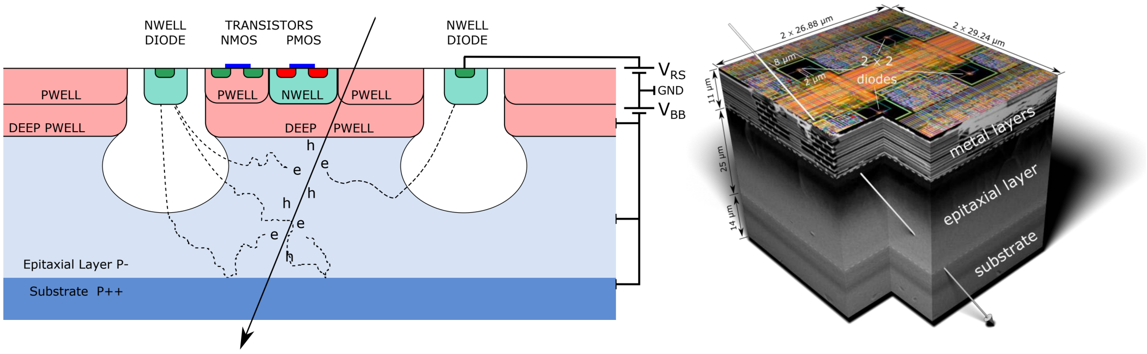

(a) Transverse section of an ALPIDE MAPS pixel cell [20].

(b) 3D transverse section of a 2 × 2 MAPS pixel matrix belonging to the ALPIDE chip [20].

Figure 3.2: Illustrations of ALPIDE MAPS pixel cells

If a charged particle traverses the detector, as shown in figure 3.2a, it loses energy due to ionization and creates electron-hole pairs in the silicon layers. As mentioned above, electrons which are created in the epitaxial layer ($p^{-}$-doped) do not diffuse into the bottom $p^{++}$-doped layer and the p-wells ($p^{+}$-doped). Therefore, the electrons will diffuse thermally through the epitaxial layer until they reach the depletion region of the n-well diode, where they are collected and start drifting in the electric field. The recombination of electrons and holes can be neglected in non-irradiated detectors. Electrons which are created in the p-wells or in the bottom layer can easily diffuse into the epitaxial layer and hence can also be collected by the diode. If enough charge is collected, the signal is processed in the in-pixel circuitry (see section 3.3) and the pixel registers a hit [20, 24].

---

[3] In case of the ALPIDE the voltage is up to 1.8 V[20].

[4] Measurements with ALPIDE are performed with reverse bias voltages of up to −6 V [6]. In this thesis, a reverse bias of −6 V is used.

[5] p-type metal-oxide semiconductor

## 3.2 ALPIDE detector structure

Figure 3.2b shows the transverse section of a 2 × 2 MAPS pixel matrix belonging to an ALPIDE chip. A single ALPIDE pixel cell has the dimensions 29.24 µm × 26.88 µm (X x Y) and a thickness of 50 µm. The thickness of the sensitive epitaxial layer amounts to 25 µm. On top of the implants of the epitaxial layer are metal layers, which provide the in-pixel circuitry and are responsible for the signal transfer to the chip logic. The pixel structure continues in X- and Y-direction creating a pixel matrix. An entire ALPIDE chip measures 3 cm × 1.5 cm and contains 524 288 sensitive pixels arranged in a matrix of 1024 columns (X) and 512 rows (Y). The chip matrix structure from the circuits side is shown in figure 3.3a. Looking at the figure, the pixel rows are numbered from 0 to 511 arranged from the top to the bottom of the chip. The columns are numbered from 0 to 1023 arranged from left to right. The row and the column of a pixel determine its address[25].

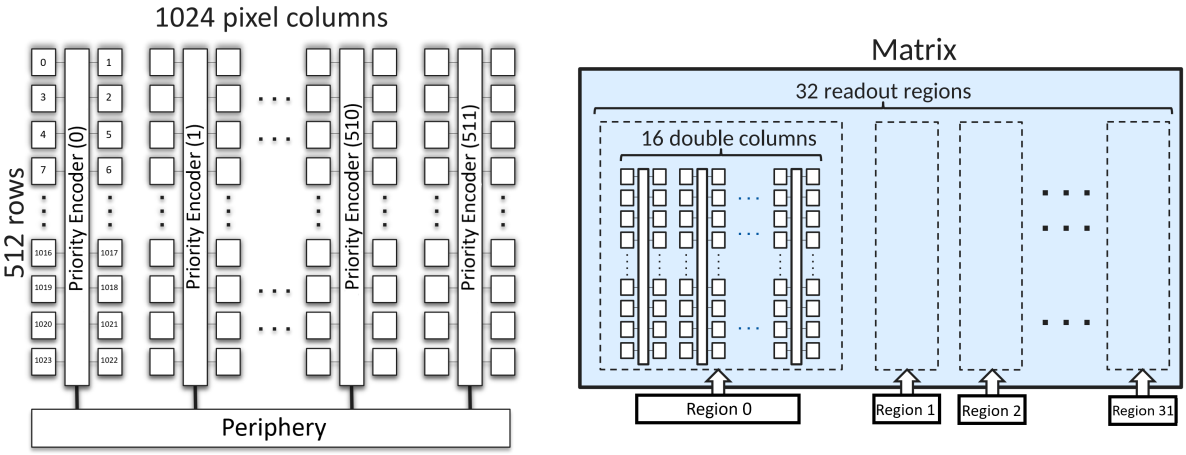

(a) ALPIDE architecture. Modified from figure in [25].

(b) ALPIDE chip regions. Modified from figure in [25].

Figure 3.3: ALPIDE structure

The readout from a pixel is executed in the first instance by the *Priority Encoder*. A Priority Encoder is connected to the pixels of two columns. Hence 512 Priority Encoders are integrated on a single chip. The two pixel columns connected by one Priority Encoder are referred to as a double column (see figure 3.3a). Every pixel of a double column has an index (see first double-column in figure 3.3a), defining the address of the pixel. The Priority Encoder selects one pixel with a registered hit in the related double-column and generates its address. The address of a pixel is sufficient to describe its state since the response of a pixel is binary - either a hit is registered or not. After the address is generated, it is transmitted further to the *periphery*. The periphery controls the entire chip and takes care of biassing and readout of the chip. After transmitting the pixel address, the Priority Encoder clears the memory and selects the next pixel of the double-column with a registered hit. This procedure repeats until the addresses of all pixels, which registered a hit, have been transmitted to the periphery and the pixel memories have been reset. Thus, the position of every pixel can be defined by the number of the double-column according to the whole chip (0 to 511 from left to right, see figure 3.3a) to identify each pixel during the readout [25].

The pixel readout on the level of the whole chip is organized in 32 regions ($512 \times 32$ pixels). Each region consists of 16 double-columns and their Priority Encoders. Every region has a readout module in the periphery, which can execute the readout of one double-column at a time in this region. Having 32 of such readout modules working in parallel allows the simultaneous readout of 32 double-columns [25].

## 3.3 Principle of operation of the in-pixel circuitry

**Signal processing** The signal processing inside a pixel and how it is controllable is now discussed. Each pixel has components which translate the charge produced by an incident particle into a readable signal for the Priority Encoder. A simplified layout of the in-pixel circuitry is shown in figure 3.4. In the input stage there is the collection diode, collecting the charge which is generated in the epitaxial layer by an incident particle. Moreover, a pulse injection capacitance is implemented to inject a voltage, which simulates an incident particle to test the in-pixel-circuitry (see section 3.4). The reset removes the voltage continuously[6], which is accumulated by an incident particle or a voltage injection.

If charge is collected or a test pulse is injected, a voltage pulse propagates into the analog front-end stage of the pixel (see figure 3.4, bottom left). The front-end stage consists of an amplifier and a discriminator, which process the signal. First, the input pulse is shaped to a signal with a peaking time of $\sim 2\,\mu s$ (see figure 3.4, bottom middle). In the discriminator the signal is compared to an adjustable threshold. If the signal exceeds the threshold, a discriminated pulse with a typical duration of up to $10\,\mu s$ is passed to the next stage. In the last stage the signal is stored in the in-pixel memory. The in-pixel memory consists of three hit storage registers which are referred to as *Multi Event Buffer* (MEB). To store the hit information in the MEB, a strobe signal is applied additionally to the discriminator output. If the two signals are in coincidence (see figure 3.4, bottom right), the discriminator output state is latched into one of the registers. Now the hit information can be read out by the Priority Encoder.

---

[6] Figure 3.4 (bottom left) shows the voltage accumulation over the period $t_f \simeq 10\,\text{ns}$ and the subsequent reset to the regular voltage over the period $t_r > 100\,\mu s$. This results in a voltage pulse

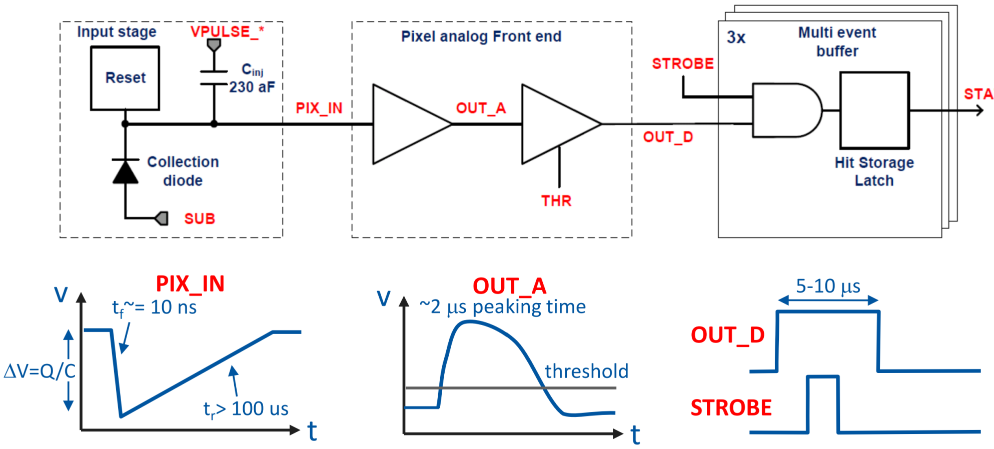

Figure 3.4: Schematic illustration of the ALPIDE in-pixel electronics and signal shaping [25].

**Digital-to-analog converter** In the front-end of each pixel, several Digital-to-Analog Converters (DAC) exist to adjust bias voltages and currents. For instance, the signal shape or the threshold can be tuned by changing the 8-bit DAC parameters (number from 0 to 255). The DACs are controlled globally for the entire chip, meaning if one DAC is changed, it will be changed for all pixels on the chip. A detailed scheme of the analog front-end of a pixel is shown in figure 3.5. In total 11 DACs are located in the pixel front-end. The threshold is controlled by three different DACs: $VCASN$, $ITHR$, and $IDB$. $VCASN$ influences the baseline voltage proportionally. This means that for increasing $VCASN$ the baseline voltage increases and, hence, the threshold decreases. ITHR determines the shape of the amplified signal (see figure 3.4, bottom middle). For higher $ITHR$ the pulse width and height are reduced. This results in an increasing threshold for increasing $ITHR$. $IDB$ controls the current through its transistor (M7, see figure 3.5) proportionally. A signal passes only to the $PIX\_OUT\_B$ node if the charge deposit from a traversing particle is sufficiently high to overcome the current setting IDB of M8. Hence the threshold increases for higher IDB [25].

To determine the threshold, the injection of a variable amount of charge into the front-end is necessary (see section 3.4). This is done by analog pulsing. In this process a voltage is applied to the capacitor $C_{inj}$ (see figure 3.4). The voltage pulse is defined as the difference between the parameters $VPULSE\_HIGH$ and $VPULSE\_LOW$. Both have a maximum value of 1.8 V and are set by 8-bit DACs. Hence the voltage can be varied in steps of 7 mV which corresponds to 10 electron charges ($e^-$), considering the nominal value of $C_{inj} = 230\,\text{aF}$ [25].

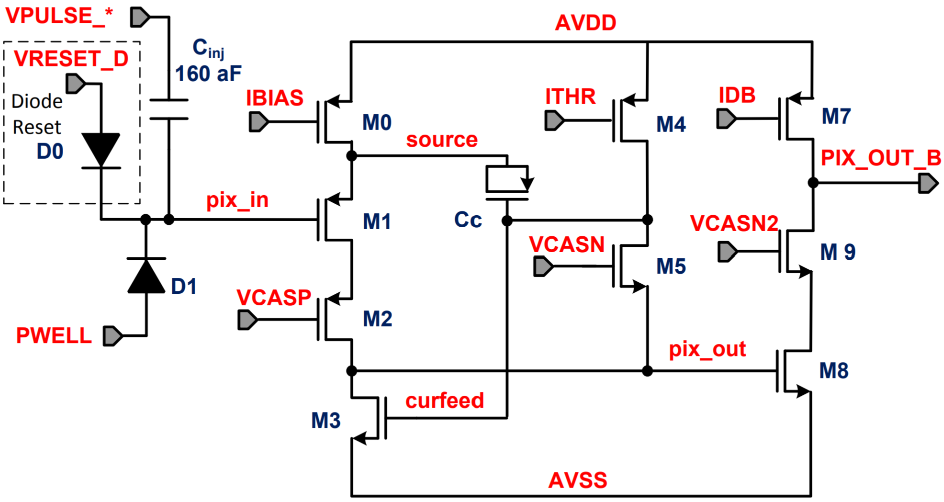

Figure 3.5: ALPIDE analog front-end scheme [25].

## 3.4 Chip tests

**Threshold test** One of the key parameters to control the chip performance is the charge threshold. In general, a threshold defines a minimal physical value that has to be supplied to a system to trigger a specific reaction. In this case, the threshold defines the minimum charge needed to trigger a hit. On the ALPIDE sensor, the threshold can be determined for each pixel of the chip. As discussed in section 3.3, the in-pixel threshold is controlled by the parameters $VCASN$, $ITHR$, and $IDB$. These DACs are set the same to all pixels, as mentioned above. To determine the threshold for a given set of these parameters, a test charge can be injected by analog pulsing (see section 3.3). A threshold test performs multiple charge injections for each tested pixel. The amount of injected charge $Q_{\text{inj}}$ varies in an adjustable range [25, 20]. For example, charges can be injected in the range of 0 to 200 electron charges in steps of 10 electron charges (in DAC values: from 0 to 20 in steps of 1). For every charge configuration, the injection is repeated $N_{\text{inj}}$ times. For each test charge configuration $Q_{\text{inj,i}}$ a number $N_{\text{hit,i}} \leq N_{\text{inj}}$ of injections result in a pixel hit. For small test charges, almost no pixel hits occur. With increasing amounts of charge, the number of pixel hits rises until it reaches the maximum number of $N_{\text{inj}}$. This can be seen in figure 3.6.

Here, the ratio of hits $N_{\text{hit,i}}/N_{\text{inj}}$ of one pixel is plotted as function of the injected charge $Q_{\text{inj,i}}$. In an ideal case, a step-function-distribution could be expected. But due to the random thermal motion of charge carriers and the resulting signal noise,

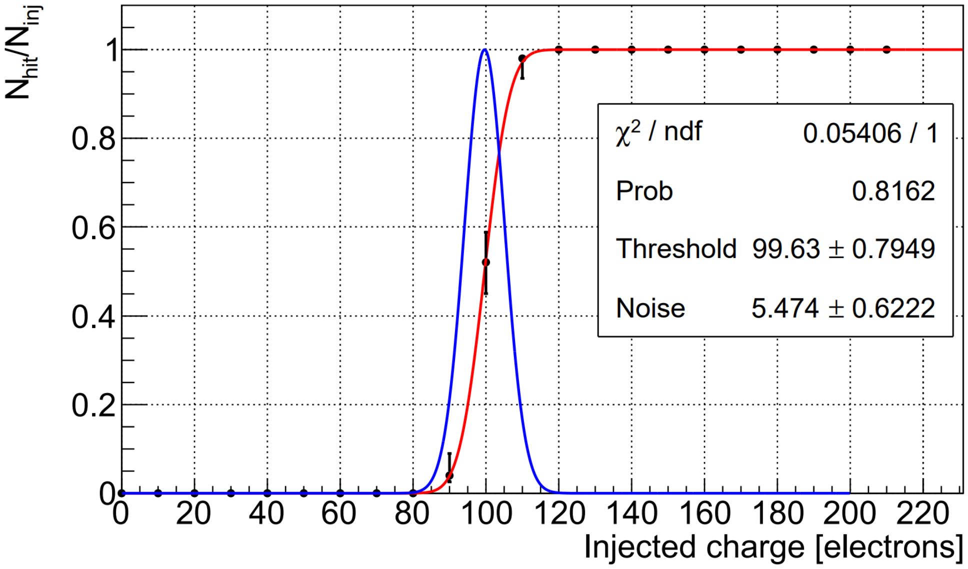

Figure 3.6: Example of the threshold measurement of one pixel: $N_{\text{hit,i}}/N_{\text{inj}}$ as a function of $Q_{\text{inj,i}}$. The red line is the error function fit. The blue line is its derivative, which is a Gaussian. The standard deviation of the Gaussian represents the electronic noise of the pixel. [20].

the distribution is smeared and shaped like a *s-curve*. Since the noise is expected to be Gaussian, the *error function* (erf) can be fitted to the data:

$$f(Q_{\text{inj}}) = \frac{1}{2}\left[1 + erf\left(\frac{Q_{\text{inj}} - \mu}{\sqrt{2}\sigma}\right)\right] \tag{3.1}$$

Here, $\mu$ represents the threshold and $\sigma$ represents the noise of the measured pixel. With the fit parameters, the threshold can be determined, which is defined as the charge at which half of the injections result in a hit ($N_{\text{hit,i}}/N_{\text{inj}} = 0.5$). Even with an identical set of parameters (DACs) for all pixels, the determined threshold can vary from pixel to pixel. This is caused by minor fluctuations during the manufacturing process of the in-pixel circuitry. Therefore the threshold for the entire chip is defined as the average of the single pixel thresholds. Usually, not every pixel of the chip is tested during the threshold test, but a fraction of a few percent of all pixels. The pixels are thereby randomly chosen out of each chip region. To control the number of tested pixels, two parameters exist. $PIXPERREGION$ controls the number of pixels per region in which the charge is injected simultaneously. Values from 1 to 32 are possible, where a value of 1 corresponds to 1 pixel per region and 32 corresponds to a complete row. The second parameter $NMASKSTAGES$ controls how often the injection of charge in a set of pixels per region (controlled by $PIXPERREGION$) is repeated. Thereby, a new random set of pixels is chosen in every repetition. To test the entire chip, the mask has to be staged $16384/PIXPERREGION$ times. Any lower number leads to a lower portion of pixels which will be scanned.

This procedure is done for every set of the parameters $VCASN$, $ITHR$, and $IDB$. By varying one parameter while the other parameters stay the same, threshold maps can be produced. These maps can be used for the chip threshold calibration afterwards.

**Noise occupancy test** Another important test for the right calibration of the chip is the noise occupancy test. In contrast to the threshold test, no charge is injected. The test just applies a selectable number of triggers $N_{\text{trg}}$ and counts the number of hits $N_{\text{hit}}$ in the absence of an external stimulus [26]. With this test the *Fake-Hit Rate* (FHR) can be determined. The FHR is defined as

$$FHR = \frac{N_{\text{hit}}}{N_{\text{pix}} \cdot N_{\text{trg}}} \tag{3.2}$$

where $N_{\text{pix}}$ represents the number of pixels of the tested chip. The dominating source of fake hits is thermal noise. The FHR depends not only on the noise but also on the threshold. As we have discussed for the threshold test, the threshold is easily adjustable and hence the FHR can be modified to a certain level. The measurable FHR is limited by the number of applied triggers $N_{\text{trg}}$. The FHR for $N_{\text{hit}} = 1$ is also referred to as *sensitivity limit*, since it is the lowest measurable FHR.

For a good threshold calibration, the FHR should be as low as possible. This means that the threshold should not be too small. At the same time, the detection efficiency should not be negatively influenced by a threshold that is set too high. The efficiency and FHR can be plotted as a function of the threshold and can be compared to find the optimal threshold for operation.

# Chapter 4

# Measurement of cosmic muons

## 4.1 Motivation

ALPIDE chips were already extensively tested and characterized in laboratories. In these tests it had been shown that the ALPIDE sensors meet and exceed the ALICE ITS upgrade requirements [6]. Several tests are performed to better understand the response of the sensors, including measurements of cosmic muons. Of particular interest are the abilities to reliably detect and track such particles, as well as qualitatively describe their influence on the detector.

In the course of this thesis, an telescope with fully characterized ALPIDE sensors was used to detect cosmic muons. Cosmic muons have some advantages compared to more commonly used radioactive sources. The expected kinetic energy of muons reaching the Earth's surface is very high (a few GeV, see section 2.2). Moreover, muons in this energy region are minimum ionizing particles and hence traverse material layers with negligible energy loss (see section 2.3). The energy loss of muons traversing the entire ALPIDE telescope ranges from 200 keV to 280 keV. The calculation is performed in section A.1.

Another advantage of cosmic muons is related to their kinetic energy. At relativistic energies muons do not scatter much and are traversing the telescope on trajectories, which can be assumed to be straight lines. This allows a simple track reconstruction, without the need of more complicated models that consider scattering.

Additionally, the known angular distribution of cosmic muons allows to test the capability of the detector of measuring the angular distribution and comparing the results with the expected one.

## 4.2 Experimental setup

The measurements were performed in an experimental laboratory at the *GSI Helmholtzzentrum für Schwerionenforschung GmbH* in Darmstadt. In the following, all important elements of the experimental setup are described. The used equipment is shown in figure 4.1.

(a) The telescope.

(b) Single ALPIDE chip.

(c) Open case of the telescope to mount the ALPIDE sensors.

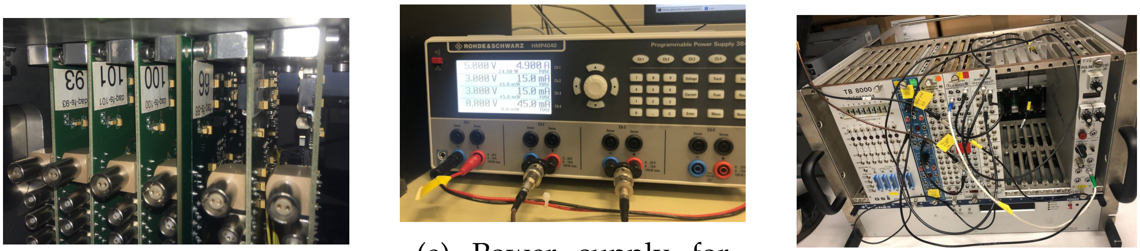

(d) DAQ boards integrated in the bottom part of the telescope.

(e) Power supply for powering the DAQ boards and ALPIDE sensors.

(f) NIM crate with several modules, including a pulser (right).

Figure 4.1: Equipment for the experimental setup.

**Telescope** The telescope, shown in figure 4.1a, contains the ALPIDE chips (see figure 4.1b), which are integrated into a compact metal case. This case is shielding the sensors from light, which could disturb the measurements. Moreover, the case ensures that the detector layers do not move relative to each other (see figure 4.1c). In total, seven ultra-thin ALPIDE sensors are integrated in the telescope, which have the dimensions 1.5 cm × 3 cm and have a distance of 2 cm from each other. Besides the ALPIDE sensors, the *Data AcQuisition* (DAQ) boards are integrated into the telescope (see figure 4.1d). Each board is directly connected to one sensor, the power supply, and the computer. The DAQ boards serve as interface between the sensors and the user. Furthermore, the DAQ boards provide all readout and control functionalities for the sensors and are powering them.

**Computer and power supply** To operate the chips of the ALPIDE telescope, the DAQ boards are connected to a computer, from which the DAQ boards are programmed. Moreover, the power supply is controllable by the computer, which enables remote access. This provides the opportunity to perform and monitor measurements from outside of the laboratory. The power supply is used to power the DAQ boards and the ALPIDE chips via their respective boards. Voltages of up to 5 V are used to power the boards and provide reverse bias voltages for the sensors (see figure 4.1e).

**NIM crate and pulser** Since ALPIDE requires a trigger and no scintillators were available to set one, a trigger signal was created by a *Nuclear Instrumentation Module* crate (NIM crate), which features a pulser and other modules necessary for the trigger logic (see figure 4.1f). The pulser creates a periodic signal of a given rate. The other NIM crate modules then process this signal to make the it readable for the DAQ boards. From the DAQ boards, a trigger signal is transmitted to the chips and and finally leads to a strobe signal, which is applied to each pixel (see section 3.3).

The trigger period of the pulser signal is set to 95.8 µs and the signal has a duration of 200 ns. The processed signal, which is sent to the DAQ boards, has a duration of 120 ns. Compared to the trigger period, the duration of the processed signal is negligible.

**Telescope orientation** The telescope is oriented such that the chips are parallel to the experimental table and perpendicular to the vertical direction- the direction in which the maximum flux of cosmic muons is expected (see section 2.2.2).

Next, the sensors are prepared for data taking.

## 4.3 Data acquisition and processing

**Preparation** The DAQ boards have to be programmed before starting the data acquisition. Afterwards, some DACs (see section 3.3) have to be adjusted to achieve a reasonable threshold at which a sensor operates with a high efficiency and a negligible fake hit rate.

After a threshold scan (see section 3.4) for the middle sensor, the chip was calibrated and the threshold was chosen at the level 127 $e^-$. For the remaining six planes, the calibration of the last experiment was maintained. The thresholds of all detector planes are shown in table 4.1:

With the external trigger the chips are programmed to operate in *triggered mode*. In this mode a strobe signal is asserted with every incoming trigger signal (see section

| Plane | Threshold $[e^-]$ |
|---|---|
| 0 | $272 \pm 6$ |
| 1 | $313 \pm 6$ |
| 2 | $228 \pm 4$ |
| 3 | $127 \pm 5$ |
| 4 | $214 \pm 5$ |
| 5 | $161 \pm 6$ |
| 6 | $202 \pm 6$ |

Table 4.1: Measured thresholds of the seven ALPIDE chips.

3.3). The strobe signal length is set to 90 µs. In this configuration the detector is almost continuously sensitive to latch an incoming hit in the in-pixel memory (Multi Event Buffer, see section 3.3).

**Data acquisition** Since muons rarely pass the telescope (see section 5.1), data must be acquired over a long period. Therefore, the measurements were conducted over a period of two weeks. The best way to operate the telescope over long time periods is via remote control since it allows to check the status of the measurement at any time.

Some issues have to be considered in the operation of the telescope in triggered mode. A trigger period of 100 µs leads to many events[1] without any pixel registering a hit. These events are not automatically deleted when taking data but are written to the file, alongside actual cosmic events. This leads to a large file size, with around 10 000 events written every second. For this reason, the file size of measurements is limited to avoid processing problems. Each file is then stored under a unique run number. After a run is finished, another one will automatically start, with the same chip settings.

The duration of a run was varied between 8 and 17 minutes, corresponding to 5 and 10.5 million events. Altogether, 352 runs valid runs, corresponding to over 89 hours of measurement, were acquired. A detailed measurement protocol can be found in the measurement protocol [27].

**Data processing** After the data acquisition, the files needed to be converted from a binary format to human readable pixel hits. This was done with the framework called *Corryvreckan* [28]. Most of the information, stored in the raw files is unnecessary for the analysis of the tracks. Therefore, it is chosen to extract

---

[1] All hits occurring during one trigger period are connected, dated with a timestamp, and referred to as *event*. If no single hit occurs during the assertion of the strobe signal, an empty event is generated for the according timestamp

only specific information about non-empty events: the event number, the chip number (the seven chips are numbered from 0 to 6), and the $x$- and $y$-coordinates of pixels (see section 3.2), which registered a hit. The event number and the chip number are important to associate hits of the same event and recognize events.

The data files were converted to text files for further analysis. In these files, all events without any registered hit were discarded, leading to a tremendous reduction of file size. The events are then analyzed using *Python* [29] and will be discussed in chapter 6.

# Chapter 5

# Theoretical calculations of the muon rate and its angular distribution

The expected detectable muon rate and its angular distribution are calculated in this chapter. The estimate of the expected results are compared to the actual outcome. This is essential to check whether the acquired data originated in expected processes, which are cosmic muons in our case, or are caused by processes that are not considered. Examples of such processes are external radiation sources located in the surrounding area or a significantly high rate of fake hits caused by either defect pixels or a poor calibration of, e.g., the threshold of a sensor. These processes would change the detection rate, leading to noticeable deviations from the expected rate.

## 5.1 Muon rate

### 5.1.1 Preliminary considerations

To determine the expected rate of detectable muons, the flux of muons traversing the detector volume is needed. Furthermore, the readout capabilities and geometry of the detector have to be considered.

The momentum spectrum is already discussed in section 2.2.2. As shown in figure 2.3a, the spectrum is nearly flat until 1 GeV/c and starts to decrease for increasing momenta. The mean energy of cosmic muons at sea level is 4 GeV. Moreover, the overall angular distribution at sea level follows approximately a $cos^2(\theta)$-distribution, where $\theta$ represents the zenith angle [11].

As already described in section 2.3, heavy charged particles lose energy primarily through the process of ionization over a wide momentum range, which is defined by the Bethe-Bloch formula (equation 2.3). Using this formula and looking at the mass stopping power plot for muons (figure 2.4a), it can be seen that the energy loss minimum is located around a muon momentum of 0.3 GeV/c to 0.4 GeV/c, depending on the traversed material. Such charged particles with a momentum in the region of minimum energy loss by ionization are called minimum ionizing particles (MIP). With increasing momentum the energy loss slowly increases up to the momentum range of a few 100 GeV/c. For even higher momenta, radiative processes start to dominate (see figure 2.4b) and lead to a steeper rise of the energy loss, which is not included in the Bethe-Bloch-formula anymore. Based on that, most cosmic muons, which can be detected on sea level, are in the energy regime from 0.3 GeV/c to 100 GeV/c, losing only a small fraction of their energy (a few MeV/cm) [15].

With this input, the muon energy loss can be estimated, depending on the setup and environment the setup is located. As calculated in A.1, muons traversing the telescope lose at most 280 keV. Therefore, the muon energy loss is negligible small compared to its total energy.

Before traversing the telescope, the cosmic muons have to pass the roof of the experimental hall (see section 4.2), which mostly consists of concrete. Since the exact composition and thickness of the roof is unknown, a concrete roof of 1 meter thickness is assumed. As shown in table 5.1, the energy loss of muons traversing 1 m of concrete with a density of $2.3\,\mathrm{g\,cm^{-3}}$ ranges from 390 MeV to 640 MeV in the considered muon energy region.

| Kinetic energy [GeV] | Mean energy loss [$\mathrm{MeVcm^2/g}$] | Mean energy loss per meter [MeV] |
|---|---|---|
| 0.293 (MIP) | 1.711 | 394[1] |
| 1 | 1.834 | 422 |
| 100 | 2.775 | 638 |

Table 5.1: Mean energy loss of muons traversing concrete [30].

It is also shown that muons with a momentum of less than 1 GeV/c lose a significant amount of their energy. Since the roof composition and thickness estimate is vague, the energy loss of muons can deviate from the stated values in table 5.1. However, most muons with a momentum of less than 1 GeV/c will not reach the detector. Consequently, muons in the momentum range of 1 GeV/c to 100 GeV/c will be considered for the following calculation.

In literature, the rate of cosmic muons is given as *absolute vertical integrated intensity* ($I_v$), which is the rate of muons traveling perpendicular to the Earth's surface and traversing a unit area. This intensity is measured with a minimum momentum threshold, which is chosen depending on the properties of the setup used for

---

[1] Since the energy loss per meter is higher than the kinetic energy of the particle, it will deposit all its kinetic energy in the material.

the measurement. With different thresholds, usually varying between 0.3 GeV/c and 7 GeV/c, the measured intensity can vary significantly [13]. Due to the considerations made above, a reasonable threshold is 1 GeV/c, which yields the absolute vertical integrated muon intensity of [13]

$$I_v = (7.58 \pm 0.40) \times 10^{-3}\,\mathrm{cm}^{-2}\,\mathrm{s}^{-1}\,\mathrm{sr}^{-1} \tag{5.1}$$

With the intensity and angular distribution of muons traversing a unit area, the rate of muons traversing the detector can be estimated. It is assumed that every cosmic muon traversing an ALPIDE sensor is detectable, which is close to the true performance for high energetic charged particles [23].

Next, the geometry of the ALPIDE telescope has to be considered, which is described in section 4.2. As stated there, the seven ultra thin sensors with dimensions of 1.5 cm × 3 cm have a distance of 2 cm from each other. With this geometrical conditions, the rate of muons traversing the detector planes can be estimated now.

### 5.1.2 Estimated total flux

**Flux through one detector layer** First, the muon flux through one single plane is calculated. The flux per unit area can be expressed as

$$\Phi = \int I(\theta)\cos(\theta)d\Omega \tag{5.2}$$

Here, $\theta$ is the zenith angle, $I(\theta)$ is the muon intensity as a function of the zenith angle

$$I(\theta) = I_v \cos^2(\theta) \tag{5.3}$$

and $d\Omega$ is the differential solid angle, described by

$$d\Omega = \sin(\theta)d\theta d\varphi \tag{5.4}$$

Here, $\varphi$ represents the azimuthal angle. The solid angle can be illustrated by looking at a segment of a unit sphere, as shown in figure 5.1a. The solid angle of the sphere's whole surface area would be $\Omega = 4\pi$ sr.

For the experimental setup, the absolute muon flux through one detector layer can be calculated with equation (5.2). Every point on the sensor accepts particles from all directions with the zenith angle $\theta$ ranging from 0 to $\frac{\pi}{2}$ representing a half-sphere. In that case, the flux is calculated by:

$$\begin{aligned}
\Phi &= \int_0^{2\pi}\int_0^{\frac{\pi}{2}} I(\theta)\cos(\theta)\sin(\theta)d\theta d\varphi && (5.5)\\
&= 2\pi\int_0^{\frac{\pi}{2}} \left(I_v\cos^2(\theta)\right)\cos(\theta)\sin(\theta)d\theta && (5.6)\\
&= I_v\frac{\pi}{2}\left(1-\cos^4(\frac{\pi}{2})\right) && (5.7)\\
&= (11.9\pm0.6)\times10^{-3}\,\mathrm{cm}^{-2}\,\mathrm{s}^{-1} && (5.8)
\end{aligned}$$

The uncertainty is calculated by Gaussian error propagation considering the uncertainty of $I_v$ (5.1). Next, the acceptance has to be taken into account. Therefore, the flux is multiplied with the considered sensor area $A = 4.5\,\mathrm{cm}^2$ to get the rate $C$

$$\begin{aligned}
C &= \Phi\cdot A && (5.9)\\
&= (53.6\pm2.7)\times10^{-3}\,\mathrm{s}^{-1} && (5.10)
\end{aligned}$$

**Flux through two detector layers** For a muon traversing more than one plane, the calculation becomes more complicated. If now two detector planes are considered, not every muon passing the first plane will also pass the second one. To take this requirement into account, the considered solid angle needs to be modified. Therefore, the solid angle for a point on the bottom detector layer can be calculated with the requirement that an incoming cosmic ray has to pass the upper layer. If the point in the center of the sensor is selected, the solid angle will have an upsidedown pyramid shape due to the detector geometry. For illustration, figure 5.1b shows the transverse section of the two considered detector planes with the maximum zenith angle for two different points on the bottom detector. In blue, the maximum zenith angle $\theta_1$ for particles passing through the center of the bottom layer is depicted.

Besides the point in the center, the maximum zenith angle $\theta_2$ fo a point near the edge of the bottom layer (green) is depicted. The zenith angles at which the muons can pass both this point and the upper detector plane are different and due to the zenith angle dependence, the flux for this configuration will differ from the flux of the previous case. Taking this flux variation into account would significantly complicate the calculations.

Going back to the three dimensions, another issue in the calculation is the shape of the detector. The rate of muons traversing the detector varies not only for different zenith angles but also for different azimuthal angles, due to the rectangular shape of the detector. Hence, the calculation would become even more complicated.

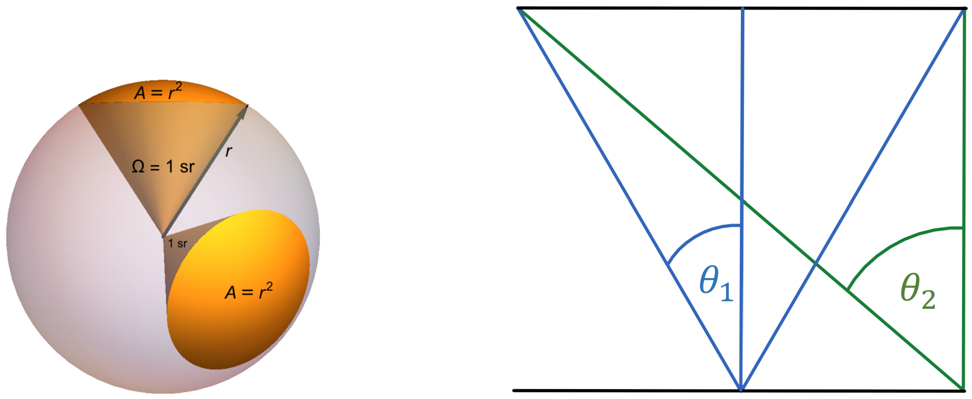

(a) Illustration of two solid angles of one steradian from different directions in a sphere, taken from [31].

(b) Transverse section of two planes with indicated solid angles for the center (blue) and the edge (green) of the detector. $\theta_1$ and $\theta_2$ are the maximum zenith angles for the center and the edge, respectively.

Figure 5.1: Illustration of the solid angle on a sphere and on a transverse section of two planes.

To simplify the calculation but still determine a reasonable estimate for the flux through the detector, two simplifying assumptions are made:

- The solid angle is constant for all points on the bottom layer, equaling the solid angle at the bottom layer's center.
- The detector layers are circular- instead of rectangular- shaped and have the same surface area as the original rectangular detector.

The first assumption allows calculating the flux for any point on the bottom detector layer in a similar way as in equation (5.5). In contrast to equation (5.5), the solid angle has to be modified due to the requirement for muons to pass both detector layers. This assumption is valid because of the small intensity variations for small angles. This is true for the telescope, which accepts only particles with relatively small zenith angles. Especially for muons traversing the whole telescope with a maximum possible zenith angle of approximately 11°[2], the intensity variation at different points on the detector can be neglected. As given by equation (5.3), the muon intensity at this angle is still over 93% of the intensity $I_v$ of vertical incoming muons. Furthermore, most particles traverse the detectors at even smaller angles since muons with large incident angles have less possible trajectories to traverse the planes. This can be seen in figure 5.1b. Here, muons with a large zenith angle like $\theta_2$ traversing both sensors can only be detected at

---

[2] The calculation can be found in the appendix A.2.

the edges of the bottom detector. On the other side, muons with small incident angles can be detected in over the full area of the detector.

The second assumption comes into play for the solid angle modification, which simplifies the solid angle shape from a pyramid to a cone. Like the first assumption, this one is also valid, because of the small angles and hence small intensity variations of incident particles appearing in the setup.

Taking these assumptions into account, the solid angle for any point on the bottom layer can be calculated with

$$\Omega_{\text{cone}} = 2\pi \int_0^{\theta} \sin(\theta')d\theta' \tag{5.11}$$

Here $\theta$ represents the maximum zenith angle of an incoming particle. The factor $2\pi$ results from the integration of the azimuthal angle. At this point, it is important to keep in mind that the maximum zenith angle calculated here will apply to the majority of traversing particles but is not the maximum possible zenith angle since the assumptions simplified the geometry and thus the solid angle. Considering the obtained $\Omega_{\text{cone}}$ and equation (5.2), the following formula for the flux can be derived:

$$\Phi(\theta) = I_{\nu}\, 2\pi \int_0^{\theta} \cos^3(\theta')\sin(\theta')d\theta' \tag{5.12}$$

$$= I_{\nu}\, \frac{\pi}{2}\left(1 - \cos^4(\theta)\right) \tag{5.13}$$

It can be seen that $\theta$ is the only unknown variable left to determine. To determine $\theta$, the distance $\Delta s$ between the layers and the diameter for the modified detector geometry needs to be calculated. The distance $\Delta s$ of two consecutive planes is 2 cm. A circular-shaped detector with the same surface area $A = 4.5\,\text{cm}^2$ as the original detector has a radius of

$$r_{\text{detector}} = \sqrt{\frac{A}{\pi}} \tag{5.14}$$

$$\simeq 1.2\,\text{cm} \tag{5.15}$$

Based on simple geometric considerations, the following equation determines the zenith angle for two nearby planes:

$$\theta = \arctan\left(\frac{r_{\text{detector}}}{\Delta s}\right) \tag{5.16}$$

Plugging in the numbers results in a maximum zenith angle $\theta = 30.96°$, a flux $\Phi(\theta) = (5.47 \pm 0.28) \times 10^{-3}\,\mathrm{cm}^{-2}\,\mathrm{s}^{-1}$, and the particle rate $C = (24.6 \pm 1.3) \times 10^{-3}\,\mathrm{s}^{-1}$.

**Flux through three or more detector layers** Next, the calculation through three or more planes is done since the most interesting results are events where muons traverse many planes. In events with up to seven traversed planes, a particle track can be reconstructed with more precision and hence confirm more reliably that a real traversing muon was detected.

Since it is expected that muons at relativistic energies do not scatter much, it can be assumed that the cosmic muons are traveling in straight tracks. As a result, the flux of muons traversing more than two planes can be treated the same way as muons traversing only two planes. The inner detector layers can be ignored since they will be crossed in any way. This concept is illustrated in figure 5.2 for muons traversing the setup with seven planes. Due to this consideration, the flux for a *n-plane-event*, in other words, an event in which n (number ranging from 2 to 7) detector planes are traversed by a particle, can be calculated in a similar way as a 2-plane-event. The only difference is the distance between the outermost planes of the event.

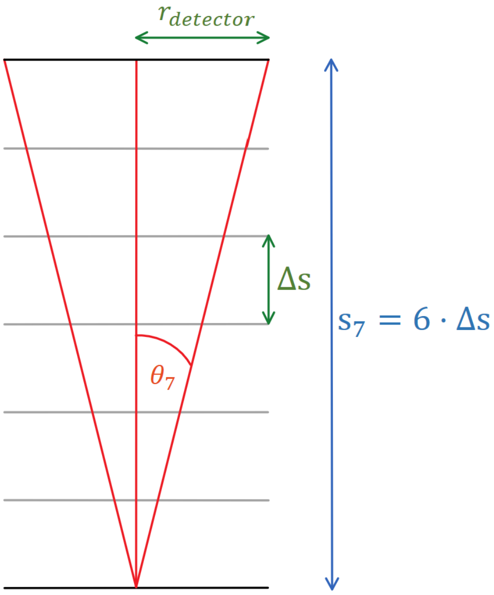

Figure 5.2: Sketch of the experimental setup with indicated maximum zenith angle for a 7-plane-event, detector radius, and detector layer distances.

The distance $s_7$ between the outermost planes for a 7-plane-event is six times the distance of a 2-plane-event and can therefore be expressed by $s_7 = 6 \cdot \Delta s$. A more general expression for the distance $s_n$ between the outermost planes of an n-plane-event is

$$s_n = \Delta s \cdot (n-1) \tag{5.17}$$

Finally, it remains to modify equation (5.16) to account for the general $s_n$

$$\theta_n = \arctan\left(\frac{r_{\text{detector}}}{s_n}\right) \tag{5.18}$$

and in consequence to account for the zenith angles $\theta_n$ in equation (5.12):

$$\Phi_n(\theta_n) = I_v 2\pi \int_0^{\theta_n} \cos^3(\theta)\sin(\theta)d\theta \tag{5.19}$$

$$= I_v \frac{\pi}{2}\left(1 - \cos^4(\theta_n)\right) \tag{5.20}$$

Now, using equation (5.19) for 2- to 7-plane-events and equation (5.5) for 1-plane-events, the zenith angles, the flux, and the rate $C$ (equation 5.9) are calculated and shown in table 5.2.

| $n$ | $\theta_n$ [°] | $\Phi_n(\theta_n)$ [$10^{-3}\,\text{cm}^{-2}\,\text{s}^{-1}$] | $C_n$ [$10^{-3}\,\text{s}^{-1}$] |
|---|---|---|---|
| 1 | 90 | $11.9 \pm 0.6$ | $53.6 \pm 2.8$ |
| 2 | 30.96 | $5.47 \pm 0.28$ | $24.6 \pm 1.3$ |
| 3 | 16.70 | $1.89 \pm 0.10$ | $8.5 \pm 0.4$ |
| 4 | 11.31 | $0.90 \pm 0.05$ | $4.04 \pm 0.21$ |
| 5 | 8.53 | $0.518 \pm 0.027$ | $2.33 \pm 0.12$ |
| 6 | 6.84 | $0.336 \pm 0.018$ | $1.51 \pm 0.08$ |
| 7 | 5.71 | $0.235 \pm 0.012$ | $1.06 \pm 0.06$ |

Table 5.2: Calculated the maximum zenith angle $\theta$, flux $\Phi(\theta)$, and rate $C$ for muons passing through 1 to 7 planes of the telescope.

Two more aspects regarding the geometry of the setup have to be considered, to calculate the final rate of expected muons.

### 5.1.3 Detection rate of n-plane-events

One aspect of the detector geometry, which was not considered until now, is the fact that for $n < 7$, there are multiple possibilities to have a track traversing n planes.

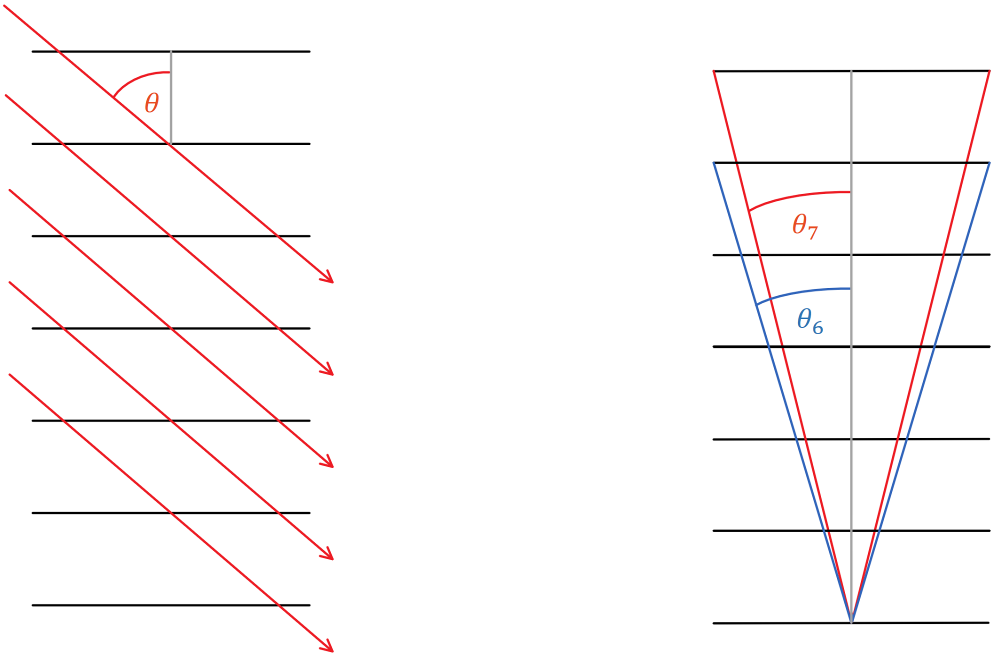

(a) Example of all possible combinations of consecutive planes leading to a 3-plane-event.

(b) Comparison of maximum zenith angles of 6- and 7-plane-events.

Figure 5.3: Sketches of the experimental setup, illustrating the multiple possibilities to traverse three detector layers and the maximum zenith angle of 6- and 7-plane-events.

For illustration, figure 5.3a shows the five possible combinations of consecutive planes, leading to a 3-plane-event. Since the vertical translation of only a few centimeters changes the flux of cosmic muons only marginally, it can be assumed to be the same flux for every configuration, equaling the flux calculated in table 5.2. Next, the number of different possible configurations, hereafter indicated as the multiplication factor M, can be calculated for any n-plane-event and is given by the following relation:

$$M_n = 8 - n \tag{5.21}$$

Taking $M_n$ into account, the detection rate $R_n$ in dependence on the flux can be calculated with:

$$R_n = \Phi_n \cdot A \cdot M_n \tag{5.22}$$

For the final calculation of the detection rate of n-plane-events, also the minimum zenith angle at which an incident particle is detectable has to be considered. To see the necessity of such a criterion, a sketch of the telescope with the solid angles for a 6- and 7-plane-event is shown in figure 5.3b. By comparing those solid angles, it can be noticed that the solid angle of 6-plane-events entirely includes the 7-plane-event solid angle. Therefore, in the previous flux calculation of 6-plane-events, muons with zenith angles smaller than $\theta_7$ were also taken into account, which would traverse all seven detector layers. This example shows that in the respective calculation the flux of an n-plane-event includes the flux of an (m)-plane-event with $n < m \leq 7$.

Now, to calculate the n-plane-event rate, excluding events with more than n planes, a minimum zenith angle will be considered in the calculation. For instance, the maximum zenith angle $\theta_7$ of a 7-plane-event limits 6-plane-events to smaller angles. Therefore, $\theta_7$ is considered as the minimum zenith angle of a 6-plane-event. Taking this additional aspect into account, $\Phi_n$ will get the final modification:

$$\Phi_n(\theta_n, \theta_{n+1}) = I_v 2\pi \int_{\theta_{n+1}}^{\theta_n} \cos^3(\theta)\sin(\theta)d\theta \tag{5.23}$$

$$= I_v \frac{\pi}{2}\left(\cos^4(\theta_{n+1}) - \cos^4(\theta_n)\right) \tag{5.24}$$

With the equations (5.22) and (5.23), the final expected rate of n-plane-events $R_n$ can be calculated and is summarized in table 5.3:

| $n$ | $\theta_n$ [°] | $\Phi_n(\theta_n, \theta_{n+1})$ [$10^{-3}\,\mathrm{cm}^{-2}\,\mathrm{s}^{-1}$] | $M_n$ | $R_n$ [$10^{-3}\,\mathrm{s}^{-1}$] |
|---|---|---|---|---|
| 1 | 90 | $6.4 \pm 0.3$ | 7 | $203 \pm 11$ |
| 2 | 30.96 | $3.58 \pm 0.19$ | 6 | $97 \pm 5$ |
| 3 | 16.70 | $0.99 \pm 0.05$ | 5 | $22.2 \pm 1.2$ |
| 4 | 11.31 | $0.380 \pm 0.020$ | 4 | $6.8 \pm 0.4$ |
| 5 | 8.53 | $0.183 \pm 0.010$ | 3 | $2.47 \pm 0.13$ |
| 6 | 6.84 | $0.101 \pm 0.005$ | 2 | $0.91 \pm 0.05$ |
| 7 | 5.71 | $0.235 \pm 0.012$ | 1 | $1.06 \pm 0.06$ |

Table 5.3: Final estimated rate of n-plane-events. In the case of 7-plane-events, the minimum zenith angle is defined as 0°.

## 5.2 Angular distribution

In this section, the calculated rates from section 5.1 will be used to calculate the expected angular distribution of traversing muons based on the detector geometry. The expected distribution can be compared to the measured data later on.

In the previous section, the minimum and maximum zenith angle for an n-plane-event is calculated to find an estimate for the rate of n-plane-events. Therefore, based on the calculations of this rate it is possible to reconstruct the angular distribution of cosmic muons from the calculated n-plane-event rate in certain angular ranges. These angular ranges are given by the minimum and maximum zenith angles.

Before calculating the angular distribution, the absolute vertical integrated muon intensity $I_v$ has to be determined, considering the calculated rate. This can be achieved by rearranging equation (5.22) to

$$\Phi_n = \frac{R_n}{A \cdot M_n} \tag{5.25}$$

With the flux and the rearranged equation (5.24), $I_v$ can be determined:

$$\begin{aligned} I_{v,n} &= \Phi_n \frac{2}{\pi\left(\cos^4(\theta_{n+1}) - \cos^4(\theta_n)\right)} \qquad (5.26) \\ &= \frac{R_n}{A \cdot M_n} \cdot \frac{2}{\pi\left(\cos^4(\theta_{n+1}) - \cos^4(\theta_n)\right)} \qquad (5.27) \end{aligned}$$

$I_{v,n}$ is the absolute vertical integrated intensity, which is calculated with the rate of n-plane-events (see section 5.1.1).

Finally, the angular distribution can be calculated by integrating $I_{v,n}$ over the angular range of $\theta_n$ to $\theta_{n+1}$ and dividing by $\Delta\theta_{n,n+1} = \theta_n - \theta_{n+1}$ to get the arithmetic mean of the detection rate for the related angular region:

$$\begin{aligned} I_n\left([\theta_{n+1}, \theta_n]\right) &= \frac{I_{v,n}}{\Delta\theta_{n,n+1}} \int_{\theta_{n+1}}^{\theta_n} \cos^2(\theta) d\theta \qquad (5.28) \\ &= I_{v,n} \cdot \left[\frac{1}{2} + \frac{\sin(2\theta_n) - \sin(2\theta_{n+1})}{4 \cdot \Delta\theta_{n,n+1}}\right] \qquad (5.29) \end{aligned}$$

In figure 5.4 the expected muon distribution with binned angular ranges is shown. Although only seven bins are shown, it agrees with the shown $\cos^2(\theta)$-distribution, which represents the expected muon distribution, without the constraints of the experimental setup. This is especially the case for small zenith angles since the calculations for these were made with small angular ranges. Hence, the bins in this region are narrow and describe the theoretical $\cos^2(\theta)$-distribution more precisely. Furthermore, the large uncertainties of the estimated rates are noticeable, which result from the Gaussian error propagation considering the uncertainty of $I_v$ (see equation 5.1).

In the following chapter, the analysis of the acquired data is explained, and the results are compared to the expected muon rate and the angular distribution calculated in this chapter.

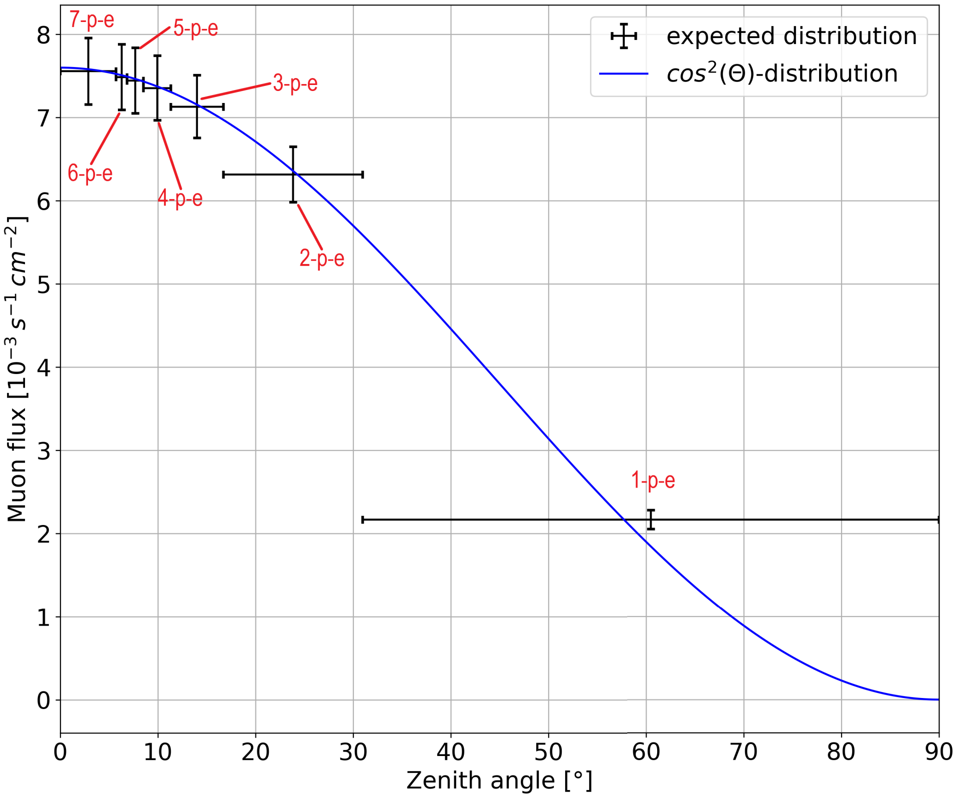

Figure 5.4: Expected angular distribution of muons with discrete angular ranges. Every bin represents the mean rate over the whole angular range (indicated by the bin width), corresponding to the angular ranges of n-plane-events (n-p-e). As comparison, the expected $cos^2(\theta)$-distribution of muons is shown, which does not account for the constraints of the setup.

# Chapter 6

# Analysis of the angular distribution

The aim of the thesis is to analyze acquired data from the ALPIDE telescope and calculate the angular distribution of the detected cosmic muons, which can be then compared to the expected distribution.

First, for each event the information about which detector planes registered a hit is extracted. Here, the information of the exact coordinates of the hit on each detector plane was not considered. With this information, the rate of n-plane-events (see section 5.1) can be determined. This quantity can be then compared to the expected rate to ensure that the detector is working properly. Moreover, a first rough estimate of the measured angular distribution can be determined with the calculation performed in section 5.2.

In the second step, the muon tracks were reconstructed, using the coordinates of the pixels that registered a hit. With this method a more precise determination of the angular distribution is achievable and can be compared to the literature.

## 6.1 Event-based analysis without tracking

The analysis of the data starts with the extraction of the registered hits and their corresponding detector layers for each event. Therefore, a custom algorithm was implemented using the programming language *Python* [29]. The algorithm first searched all events for the number of planes that had pixels firing (registering a hit). At this point, the sequence of the planes in the events is not considered. The number of n-plane-events and the duration ($8\,\text{min} - 17\,\text{min}$) of each run is accumulated for later analysis. In total, more than 3000 events with four or more planes registering a hit were detected. These events, which involve multiple detector layers, are of special interest since they originated most probably from a charged particle. The reason is that it is very unlikely that uncorrelated hits occur

on multiple sensors at the same time[1]. The amount of events with at least four planes is sufficient to obtain an adequate statistical base for further calculations. The total number of events is shown in figure A.1.
With the number of n-plane-events per run and the duration of the corresponding run, the rate of n-plane-events can be determined for each run. Next, the arithmetic mean of the rate is calculated and plotted alongside the expected mean rate, shown in figure 6.1. Both distributions are very similar, and the measured rates are within close range to the expected rates, except for the 1-plane-events. It is apparent that also the rates of 2-, 3- and 6-plane-events do not agree within the range of uncertainties, while the rates of 4-, 5-, and 7-plane-events do agree. It is further noticeable that apart from the rate of 7-plane-events, every rate is underestimated. This might indicate a systematic error.

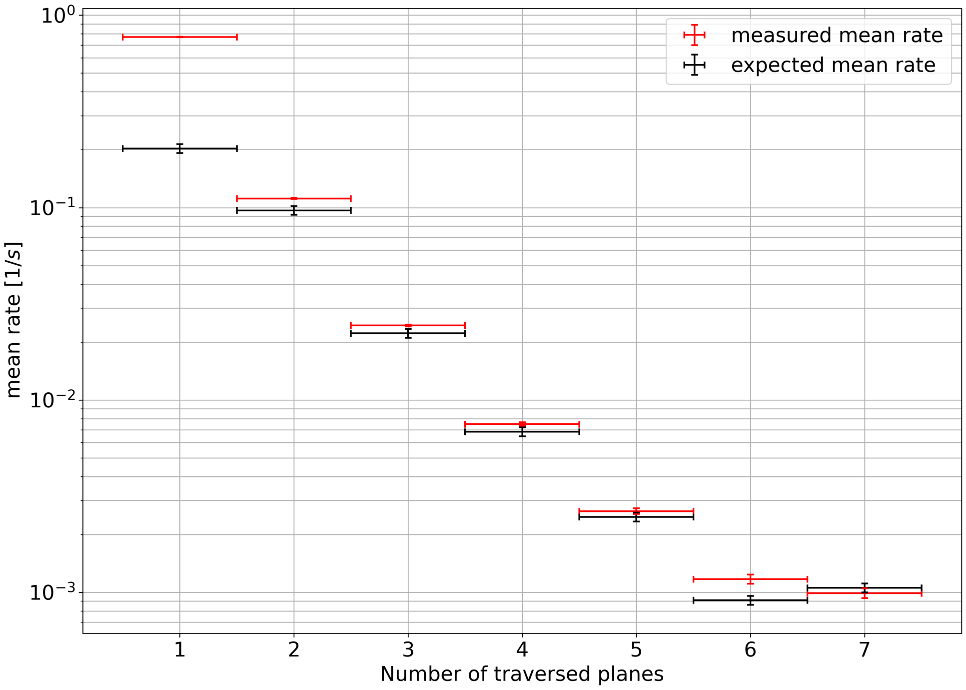

Figure 6.1: Expected and the measured mean rate of n-plane-events. The horizontal error bars indicate the bin width.

Next, to find possible sources of systematic errors, it is investigated which planes fired in an event and whether they are consecutive. A non-consecutive event is an event with a gap in the numbering sequence of firing planes. For example, a 4-plane-event with the firing planes $1, 2, 4, 5$ is non-consecutive and cannot be classified as a 4-plane-event. Such events can be caused by, e.g., a fake hit of one

---

[1] One event accumulates all hits occurring in a time period of 90 µs (see section 4.3)

or more planes or by inefficiencies, meaning that one plane which is traversed by a particle did not register a hit. Gaps cannot appear in 1- and 7-plane-events since 1-plane events have no sequence of multiple detector layers, and 7-plane events include all detector layers, and thus, no detector layer can be missing from the sequence.

In figure 6.2 (left), the rate of n-plane-events with at least one gap is shown and compared with the total rate of measured n-plane-events. On the right, the ratio of non-consecutive events to all detected events is plotted. The percentage of non-consecutive n-plane-events increases continuously for events with more planes, in particular for events including 3 or more planes. Around 13 % of the 6-plane-events include a gap, which is a significant amount.

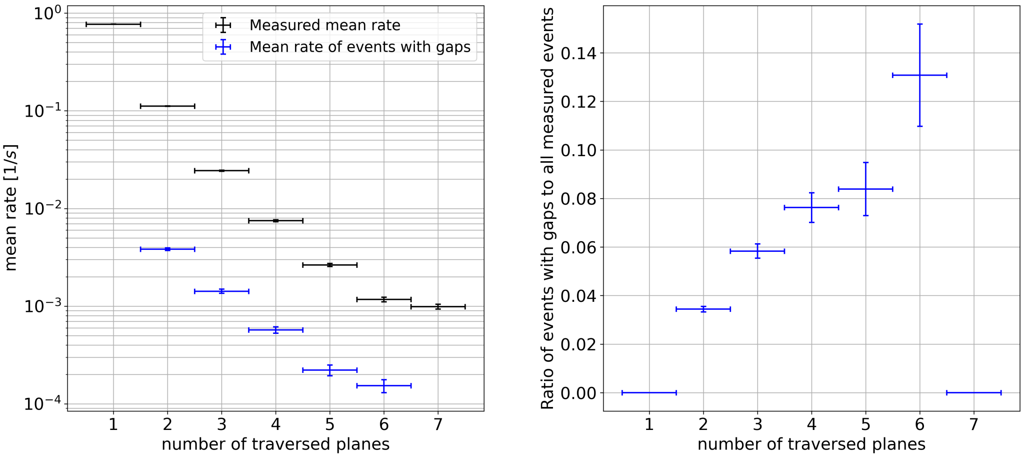

Figure 6.2: Mean rate of measured n-plane events, considering non-consecutive n-plane-events. The horizontal error bars indicate the bin width. The mean rates of the total measured n-plane-events and the non-consecutive n-plane-events are compared (left), and the ratio of the two rates is shown (right). For 1- and 7-plane-events only consecutive tracks occur.

Since there are several possible causes for a gap, the best way to handle these events is to exclude them from the calculation. Therefore, the previously determined rate of measured n-plane-events can be corrected by subtracting the rate of non-consecutive n-plane-events from the total rate. Figure 6.3 shows the rates from figure 6.1 alongside with the rate corrected by removing non-consecutive events. 1-plane-events are excluded since the correction does not apply to them, and the analysis is focused on events with multiple planes, which most probably originated from charged particles and not from noise, as a significant amount of 1-plane-events does. The correction has a noticeable impact, bringing the measured mean rate closer to the expected rate. Especially the rate of 6-plane-events, which clearly differs from the expectation in figure 6.1, agrees with the expected rate now.

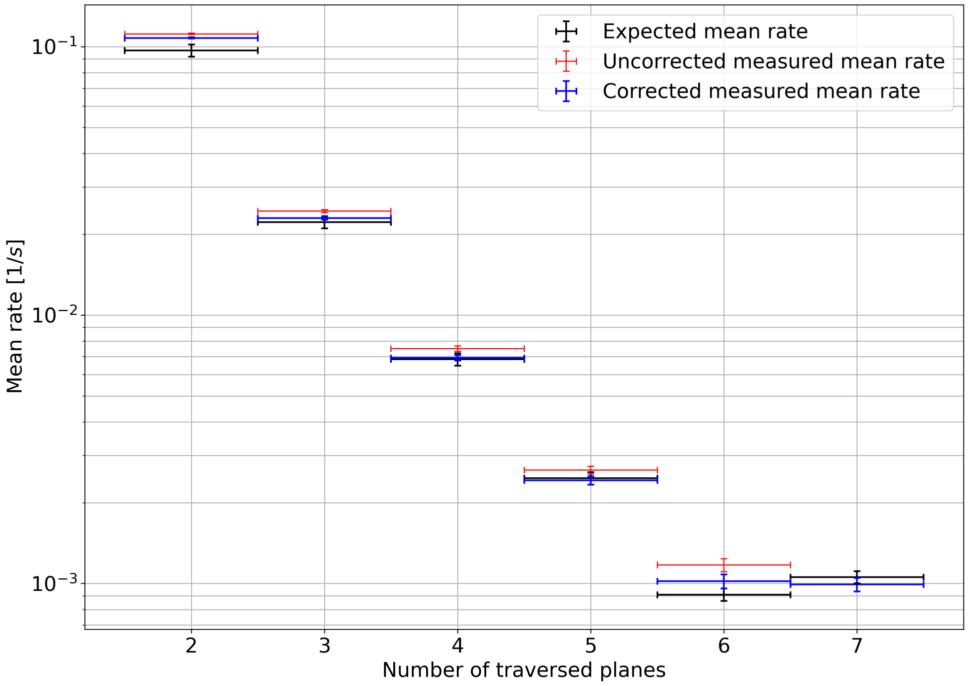

Figure 6.3: Correction of the measured mean rate by removing non-consecutive n-plane-events. The horizontal error bars indicate the bin width.

Using the results shown in figure 6.3, an estimate of the measured angular distribution of cosmic muons can be calculated. As discussed in section 5.2, the determined rate of n-plane-events $R_n$ is inserted in equation (5.25) to calculate the particle flux $\Phi_n$. The flux is used to calculate the vertical integrated intensity $I_{v,n}$ of muons for each angular range (equation 5.26). Using $I_{v,n}$, the angular distribution can be calculated with equation (5.28).

The results are plotted in figure 6.4 and compared with the expected distribution. For the same reason as for figure 6.3, the results from the 1-plane-events are excluded, which would represent the flux in the range of 30.96° to 90° based on the setup geometry (see 5.2). The comparison shows that the measured distribution is in agreement with the expected one. The high uncertainties of the distribution are caused by the low number of events in each bin. Hence, the precision of the distribution calculated with this method could be improved by more statistics.

In order to verify that the tracks originated from cosmic muons and to determine a more precise angular distribution, further analysis is carried out.

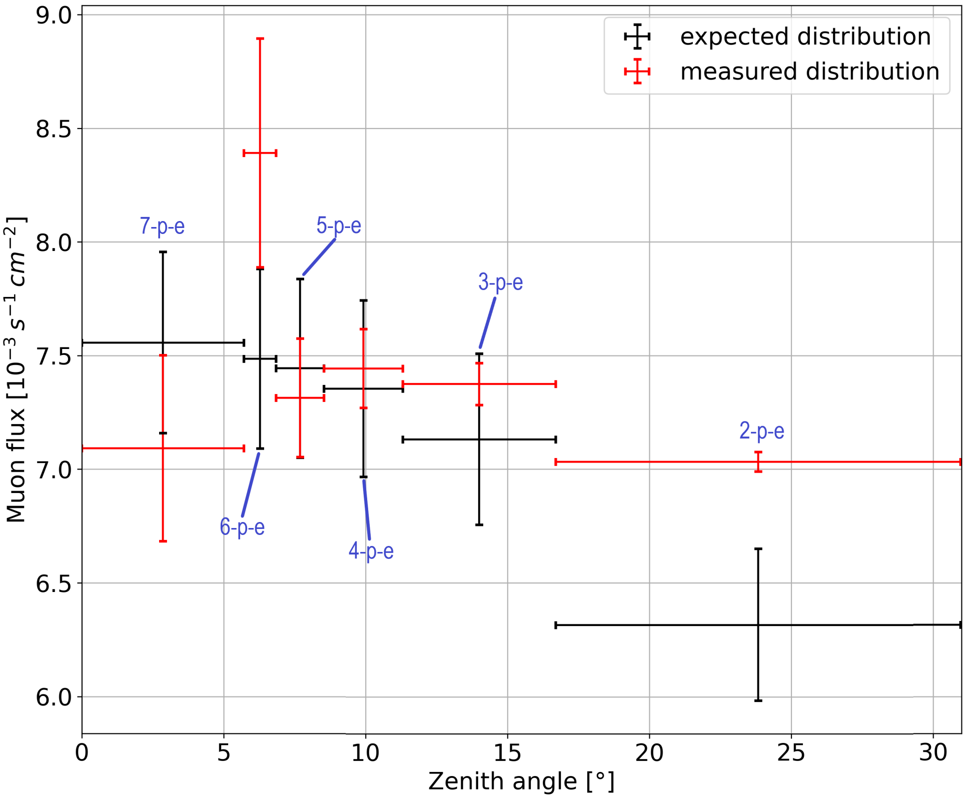

Figure 6.4: Comparison of the measured and the expected angular distribution based on the rate of n-plane-events. Every bin represents the mean rate over its whole angular range (indicated by the bin width), corresponding to the angular ranges of n-plane-events (n-p-e).

## 6.2 Tracking based analysis

To further analyze the data, the tracks of the cosmic muons have to be reconstructed from hits on the detector planes. Therefore, the coordinates of firing pixels were extracted from the data files. This provides the track position on the pixel matrix in the $x-y$-plane (see section 3.2). The $z$ position can be determined with the plane number of the firing detector layer[2]. If groups of pixels (clusters) on a plane fired, the $x$ and $y$ position of the hit is determined by the arithmetic mean of the $x$- and $y$-coordinates from all firing pixels of the plane. The standard deviations in $x$ and $y$ direction ($\sigma_x$ and $\sigma_y$) are also calculated, with the following relation:

---

[2] The detector layers are 2 cm apart (see figure 5.2)

$$\sigma_x = \sqrt{\left(\frac{1}{N-1}\sum_{i=1}^{N}(x_i - \bar{x})^2\right)} \tag{6.1}$$

Here, $\bar{x}$ represents the arithmetic mean in $x$ direction, $N$ represents the number of firing pixels, and $x_i$ represents the $x$-coordinate of each firing pixel. The calculation for $\sigma_y$ is performed analogously.

A track will only be further considered if the standard deviations $\sigma_x$ and $\sigma_y$ of each detector layer fulfill the requirement $\sigma_{x,y} \leq 15$ pixels. This ensures that all hits on a plane originated from the same incident particle and no distortions by random fake hits occurred. If only one pixel of a plane fired, no mean is calculated and the coordinates of the pixel are used for further analysis[3].

### 6.2.1 Alignment

The sensors can only be mounted in the telescope case with limited precision, and hence a shift in x and y direction can occur between the layers. Therefore, a software-based alignment of the detector planes needs to be performed before the tracks can be reconstructed properly. In this process, a global coordinate system is used, which relates the $x$- and $y$-coordinates of each plane in the telescope.

The data from cosmic measurements is not used to perform the alignment due to the insufficient amount of events. Instead, the data from a testbeam is used for the alignment. Data from testbeams have the advantage that particle beams hit the detector perpendicular to the detector layers, which is optimal for the alignment of the layers. Another advantage is the good statistics, which can be relied on.

A disadvantage might be that the detector setup was moved between the time the testbeam took place and the conducted cosmics experiment. Therefore, the position of the detector layers might have changed, and hence the performed alignment may not apply to the setup.

The data of two testbeams is available, one performed before and one after the conducted experiment. The alignment for both datasets was made using the data analysis framework *Corryvreckan* [28]. Afterwards, both alignments were successively applied to the data sample acquired in the course of this thesis.

In figure 6.5 a two dimensional representation of five representative 7-plane-events is shown without alignment (left), with alignment from a testbeam performed in December 2019 (center) and with alignment from a testbeam performed in August 2020 (right). For better visualization, the consecutive planes are connected by a

---

[3] For the ALPIDE, the spatial resolution for single pixel hits per plane can be approximated with the binary resolution, which is $\frac{p}{\sqrt{12}}$, where $p$ is the pixel pitch [22]. This resolution is used to estimate the standard deviations $\sigma_{x,y}$ in the case of one firing pixel.

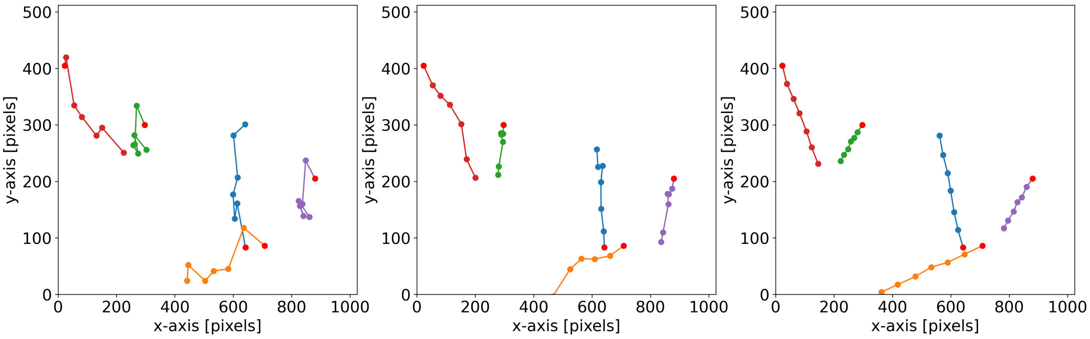

Figure 6.5: Projection of muon tracks from a representative run that shows five 7-plane-events. Consecutive planes are connected by a straight line and the first plane is marked as red. Data is shown without alignment (left), with alignment from a 2019 testbeam (center), and with alignment from a 2020 testbeam (right).

straight line. The unaligned tracks (figure 6.5, left) of these 7-plane-events have almost nothing in common with a straight line. The alignment of 2019 (figure 6.5, center) improves this condition, with some tracks appearing almost in a straight line. The alignment seems to be only sufficient in the $x$-direction, as tracks moving not perpendicular to the $x$-axis are still unaligned. Another aspect indicating that this alignment cannot be used for further analysis, is that the hits (marked as points on the track) are not equidistant. This is an essential criterion considering equidistant detector layers and that the muons are expected to travel in straight trajectories. Using the alignment of 2020 (figure 6.5, right), the tracks appear to be straight, and the hits are mostly equidistant. In contrast to the alignment of 2019, this is a significant improvement. However, small deviations are observable in the short tracks, which indicate that this alignment still does not fully apply to the cosmics data, but is a good estimate to get as close to the ideal alignment as possible.

### 6.2.2 Track fitting for quality assurance

Fitting the tracks is a crucial part of the analysis to ensure that an event originated from a muon. Figure 6.5 (right) shows the projection of a few tracks. In reality, particles travel in three dimensions; hence the true detected tracks are three dimensional. Analyzing the tracks with *Corryvreckan* [28] was complicated due to the segmented organization of the acquired data in many small files. Hence, instead of using *Corryvreckan*, it is chosen that the three dimensional tracks are projected to two dimensions[4] for the fitting procedure, as already seen in figure 6.5. In this way, a linear fit can be applied to the data with the function:

$$f(x) = a \cdot x + b \tag{6.2}$$

Here, $x$ is the projected $x$-coordinate of the track and $f(x)$ is the fit function, representing the projected $y$-coordinate, which results out of the fit. In figure 6.6 the representative 7-plane-events with an applied fit (black line) to each track are shown.

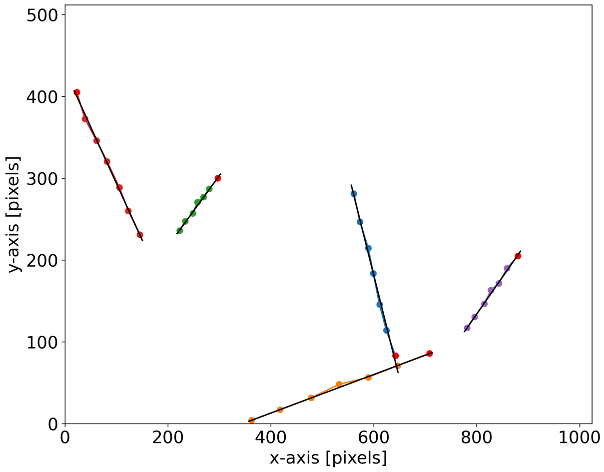

Figure 6.6: Projection of muon tracks from a representative run with five 7-plane-events. Consecutive planes are connected by a straight line and the first plane is marked as red. A linear fit, indicated by the black line, is applied to every track.

The fit is used in the first instance to evaluate the quality of the tracks. If the linear fit describes the track well, it originated most probably from a muon. If the fit does not apply to the track, it is probably distorted by random fake hits. Hence it does not reflect the true trajectory of the incident particle and cannot be used for the determination of the angular distribution. The evaluation of the fit quality is achieved by checking the goodness of the fits using the $\chi^2$-test:

$$\chi^2 = \sum_i \frac{(f(x_i) - y_i)^2}{\sigma_{y_i}} \tag{6.3}$$

Here, $i$ represents the plane number corresponding to the hit coordinates. To get a measure of the goodness of the fit, which does not depend on the number of planes involved in an event ($n_{\text{planes}}$), $\chi^2_{\text{red}}$ has to be calculated:

---

[4] The fitting procedure on this data can also be performed in three dimensions, as described in [32].

$$\chi^2_{\text{red}} = \frac{\chi^2}{dof} \tag{6.4}$$

Here, $dof = n_{\text{planes}} - 2$ represents the *degrees of freedom*, where 2 is the number of variables ($a$ and $b$) used for the fit function. In general, a $\chi^2_{\text{red}} = 1$ means that the applies perfectly to the data, whereas $\chi^2_{\text{red}} < 1$ indicates that the errors are overestimated, and $\chi^2_{\text{red}} > 1$ indicates that the errors are underestimated.

The quantification of the goodness of the fit is only possible for events with at least three involved planes, which corresponds to $dof = 1$. The quality of the fit improves if the number of measurements increases. Moreover, the probability that a track originated from a muon increases with the number of involved planes since other sources of hits (e.g., fake hits on multiple planes) are extremely unlikely to happen. Hence only events with four and more planes are considered in further analysis to ensure a higher quality of tracks and fits.

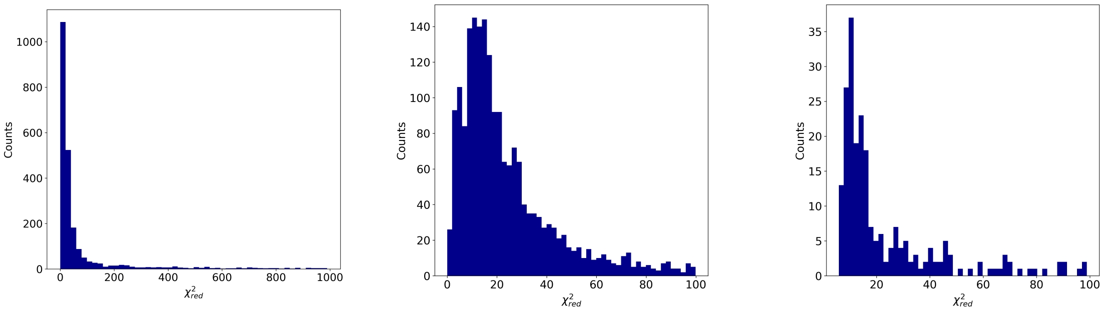

(a) 4 and more planes, $\chi^2_{\text{red}} \leq 1000$.

(b) 4 and more planes, $\chi^2_{\text{red}} \leq 100$.

(c) 7 planes, $\chi^2_{\text{red}} \leq 100$.

Figure 6.7: $\chi^2_{\text{red}}$-distributions with different ranges.

Figure 6.7 shows the $\chi^2_{\text{red}}$ distribution for different $\chi^2_{\text{red}}$-cuts and for different numbers of planes. Most events have $\chi^2_{\text{red}} \leq 100$, while a few occurring events have significantly higher $\chi^2_{\text{red}}$-values. The high $\chi^2_{\text{red}}$ values indicate a significant underestimation of the uncertainties and a bad track quality. Nevertheless, the $\chi^2_{\text{red}}$ distribution can be used to classify the goodness of events. To see if events with $\chi^2_{\text{red}} \leq 100$ can be identified as potential muon track, figure 6.8 shows a few representative tracks with $\chi^2_{\text{red}} \leq 100$ (left) and with $\chi^2_{\text{red}} > 100$ (right). Most of the tracks with $\chi^2_{\text{red}} > 100$ show no straight trajectories for muons traversing the detector. Therefore, a cut at $\chi^2_{\text{red}} \leq 100$ is applied in order to select reasonable tracks for the following calculation of the angular distribution.

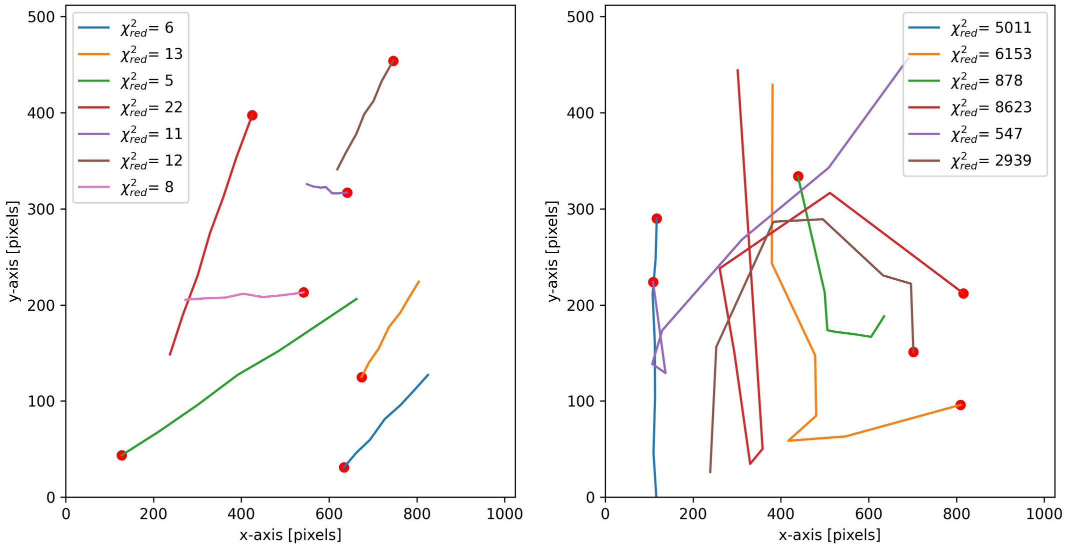

Figure 6.8: Two dimensional visualization of representative muon tracks, with the criteria $\chi^2_{\text{red}} \leq 100$ (left) and $\chi^2_{\text{red}} > 100$ (right). Consecutive planes are connected by a straight line and the first plane is marked as red.

### 6.2.3 Determining the angular distribution

After applying the $\chi^2_{\text{red}}$-cut on the data, an angular distribution analysis can be performed. The hit coordinates associated to the tracks with the $\chi^2_{\text{red}}$-cut are now considered to calculate the zenith angle $\theta$ since the fit was applied in two dimensions and does not take into account the z-axis, which would be needed to perform a reasonable calculation of $\theta$. Taking the hit coordinates from the first and last fired plane yields a good estimate of the three dimensional track since the remaining tracks after the $\chi^2_{\text{red}}$-cut are expected to be straight. $\theta$ is calculated with the following relation:

$$\theta = \arctan\left(\frac{r}{s}\right) \tag{6.5}$$

Here, $s$ represents the vertical distance between the two outermost planes[5] and $r$ represents the projected distance of the hits in the $x-y$-plane. The distance $r$ can be calculated with the relation $r = \sqrt{\Delta x^2 + \Delta y^2}$, where $\Delta x^2$ and $\Delta y^2$ are the squared differences in the $x$- and the $y$-direction of the two outermost hits. The pixel coordinates $x$ and $y$ are converted into cm before calculating the angle. Therefore, they are multiplied by their pixel pitches (29.24 µm in $x$ and 26.88 µm in $y$, see section 3.2).

---

[5] Two consecutive planes are 2 cm apart. The number of involved planes defines the distance $s$ (see figure 5.2)

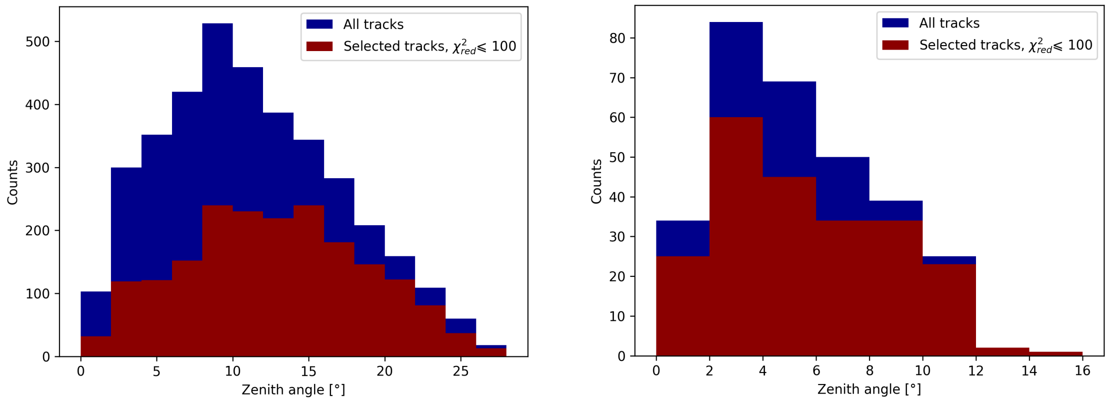

(a) All events with four or more planes.

(b) Events with seven planes

Figure 6.9: Angular distributions for tracks with and without $\chi^2_{\text{red}}$-cut binned in 2° increments.

In figure 6.9 the angular distributions of events with at least four planes (6.9a) and seven planes (6.9b) are shown with and without the $\chi^2_{\text{red}}$-cut applied to the data. Since 7-plane-events are a subset of events with four or more planes, they are included in both distributions of figure 6.9. The first thing to notice is that events at minimal angles are rare in both distributions, independent from the applied $\chi^2_{\text{red}}$-cut. The distribution in figure 6.9a is peaking in the range of 8° to 16°, while the 7-plane-events (figure 6.9b) shows a peak at 2° to 4°. After the peaks, the number of events in each bin are decreasing for increasing zenith angles. Most events at larger angles are classified as as good tracks ($\chi^2_{\text{red}} \leq 100$). At smaller angles, a larger fraction of events with high $\chi^2_{\text{red}}$ values can be observed, except for the first bin.

The detected distribution of 7-plane-events (see figure 6.9b) can be compared to the expected $cos^2(\theta)$-distribution (see figure 2.3b), up to an angle of 11.3° (see Appendix A.2). It is expected to see the majority of events at the smallest angles and a slight decrease towards higher angles. This is in agreement with the measured distribution, except for the first and second bin. While the first bin is significantly lower, the second bin is higher than expected.

Comparing the distribution in figure 6.9a, which includes 4-, 5-, and 6-plane-events, with the expected $cos^2(\theta)$- distribution is more difficult due to the geometrical constraints of the experimental setup. As discussed in chapter 5, n-plane-events with $n < 7$ have a minimum and maximum zenith angle in which it is expected to detect the majority of events. Therefore, rates of 4-, 5-, and 6-plane-events need to be further distinguished to investigate this distribution.

In figure 6.10 the angular distributions of (4+)-plane-events (events, including at least four planes), (5+)-plane-events, (6+)-plane-events, and 7-plane-events are shown. For instance, considering the second bin (2° to 4°), it can be observed that

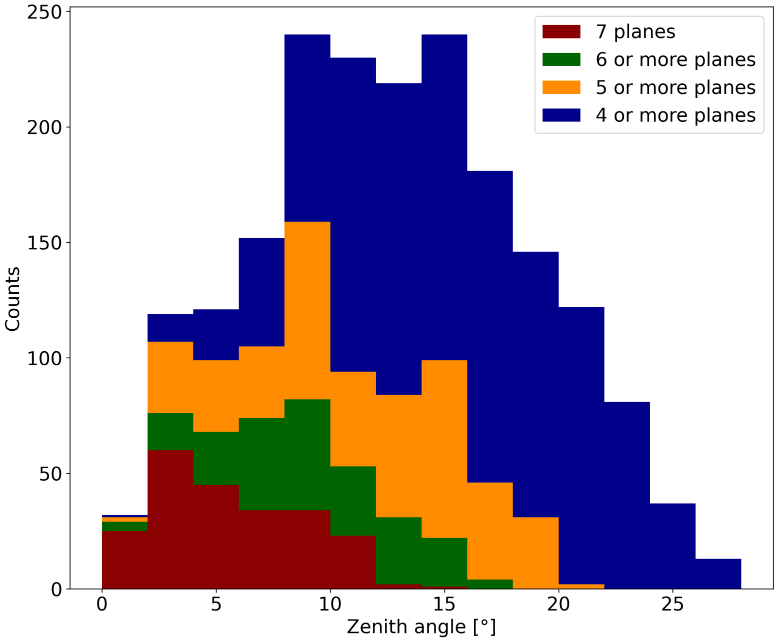

Figure 6.10: Angular distributions of events involving 4 or more planes, 5 or more planes, 6 or more planes, and 7 planes with $\chi^2_{\text{red}} \leq 100$.

there are $\sim$ 120 (4+)-plane-events. Out of these, only $\sim$ 15 are true 4-plane-events, and $\sim$ 105 are (5+)-plane-events. Again, out of these, $\sim$ 30 are actual 5-plane-events, and the remaining $\sim$ 75 are 6- or 7-plan- events. Finally, it can be seen that only $\sim$ 15 are true 6-plane-events, and the remaining $\sim$ 60 involve all seven planes.

The distribution of (5+)-plane-events and (6+)-plane-events show a peak at 8° to 10°. All four distributions show a continuous decline in the number of tracks at increasing angles after the peak.

It is noticeable that visible fluctuations in the distribution appear due to the relatively small number of events per bin. Especially the number of events in the range 0° to 4° seem to indicate a systematic error, which might be caused by misalignment. Comparing the peaks, a shift to larger angles for events with fewer planes is observable. This is in agreement with the expectations since the angular range in which n-plane-events are expected to be detected increases with decreasing n (see table 5.3).

Besides the shift of the peak of the distributions, an increasing maximum angle for decreasing n is observed. These maximum angles are more than twice as large as the angles $\theta_n$ calculated in section 5.1.2 (see table 5.3). The reason for the significant deviation is that the angles of table 5.3 are calculated under two assumptions, which are discussed in section 5.1.2.

The first assumption simplifies the calculation of the solid angle, as it is assumed to be equal to the solid angle of the bottom layer's center. In this case, the maximum zenith angle $\theta$ considered in the calculation is also determined from the sensor's center, which is smaller than the maximum angle $\theta'$ at the edge of the sensor (see $\theta_1$ (center) and $\theta_2$ (edge) for a 2-plane-event in figure 5.1b). $\theta'$ depicts the maximum possible zenith angle, at which an incident particle can traverse circular detector layers. Similar to the calculation of $\theta_n$ in equation 5.18, $\theta'_n$ of an n-plane-event can be calculated by

$$\theta'_n = \arctan\left(\frac{2 \cdot r_{\text{detector}}}{s_n}\right) \tag{6.6}$$

where $r_{\text{detector}} \simeq 1.2\,\text{cm}$ represents the detector radius and $s_n$ the distance of the two outermost planes of an n-plane-event. The resulting angles are shown in table 6.1.

Compared to $\theta_n$, the angles $\theta'_n$ are almost doubled. Moreover, $\theta'_n$ fit rather well to the measured maximum zenith angles $\Theta_n$, even though they are still significantly smaller than the measured maximum angles.

This deviation can be eliminated using the original rectangular detector geometry since it was simplified to a circular shape within the calculations of chapter 5. The maximum possible incident angle of a muon is achieved if it traverses, e.g., the top-left edge of the first sensor layer and the bottom-right edge of the last traversed sensor layer of the telescope. This angle is described by

$$\theta''_n = \arctan\left(\frac{\sqrt{x^2_{\text{detector}} + y^2_{\text{detector}}}}{s_n}\right) \tag{6.7}$$

where $x_{\text{detector}} = 1.5\,\text{cm}$ and $y_{\text{detector}} = 3\,\text{cm}$ represent the detector dimensions (see section 4.2).

The resulting angles are shown in table 6.1 and can be compared to the measured maximum zenith angles $\Theta_n$. All angles agree within the uncertainties of the measured maximum angles. It is noticeable that the deviation from the measured angles increases for decreasing n. Furthermore, every calculated maximum angle is overestimated, which can be explained by the generally low number of events per bin and the low probability of incident particles traversing the telescope at such large angles. For large zenith angles the possible orientations at which charged particles are detectable are restricted. Therefore, those particles are less probable to be detected, because the start and end points of the projections are limited to a specific region of the sensors.

| n | $\theta_n$ [°] | $\theta'_n$ [°] | $\theta''_n$ [°] | $\Theta_n$ [°] |
|---|---|---|---|---|
| 4 | 11.3 | 21.8 | 29.2 | $27 \pm 1$ |
| 5 | 8.5 | 16.7 | 22.7 | $21 \pm 1$ |
| 6 | 6.8 | 13.5 | 18.5 | $17 \pm 1$ |
| 7 | 5.7 | 11.3 | 15.6 | $15 \pm 1$ |

Table 6.1: Calculated and measured maximum zenith angles for n-plane-events with $4 \leq n \leq 7$ . $\theta_n$ is the maximum angle calculated from the circular sensor's center, $\theta'_n$ is the maximum angle from the circular sensor's edge, and $\theta''_n$ is the maximum possible zenith angle for the original rectangular detector geometry. $\Theta_n$ represents the measured maximum zenith angle based on figure 6.10.

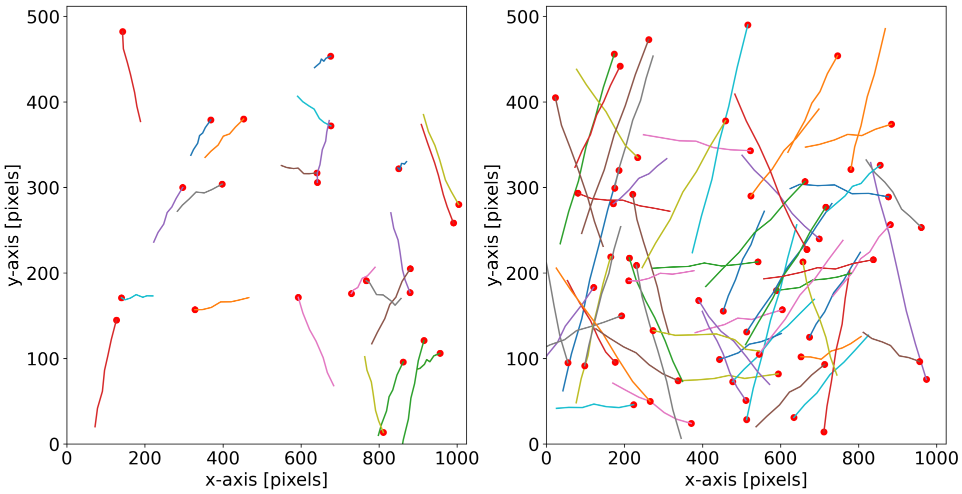

Figure 6.11: 7-plane-events, with $\chi^2_{\text{red}} \leq 100$, with a zenith angle in the range 0° to 2° (left) and 2° to 4° (right).

In the angular distributions of figure 6.10 it is desirable to further investigate the conspicuous region of the angular distributions, namely the angular range of 0° to 4°. Figure 6.11 shows 7-plane-events in this angular range, after applying the $\chi^2_{\text{red}}$-cut. As until now, the first plane of an event is marked red and the planes are connected with straight lines. In the left subplot, the tracks with zenith angles of 0° to 2° are shown. The tracks in this range seem to deviate from a straight line, especially if they are compared to the tracks with a slightly higher zenith angle of 2° to 4° (see figure 6.11, right). In this angular range the majority of tracks are almost straight lines. This confirms the suspicion that the small number of events measured with an angle of 0° to 2° could be caused by misalignment.

# Chapter 7

# Discussion and conclusion

In the course of this thesis, measurements of cosmic muons with a telescope featuring ALPIDE sensors were performed. The quality of the measurements is examined by comparing the measured muon rate with a theoretical rate, which is calculated considering the geometrical constraints that regard the experimental setup. The measured events are differentiated by the number n of traversed sensor layers and referred to as n-plane-events (n ranging from 1 to 7). Moreover, the measured angular distribution of cosmic muons at ground level is determined with two different methods and compared to the expected angular distribution.

**Event based analysis** It was found that, with the exception of 1-plane-events, the rates of detected n-plane-events are within close range to the theoretical calculation made in section 5.1. The purpose of the theoretical calculation was to examine if the measured events reflect the expected mean rate of incoming cosmic muons. The calculation of the n-plane-event rate was carried out using simplifications, with the purpose of having an estimate to compare with the measurements. The results show that the measured n-plane-event rates are in good agreement with the expected ones, showing that cosmic muons were reliably measured with the detector.

The significantly higher rate of 1-plane-events can be caused by several different effects- e.g., noisy pixels, which regularly register fake hits (see section 3.4). The direct impact of the high rate of 1-plane-events on the analysis is small since the analysis is focused on events with multiple planes, which allow the reconstruction of the tracks and incident angles of particles traversing the telescope, and consequently, are not considered in further calculations. Nevertheless, effects like noisy pixels, which lead to the high rate of 1-plane-event, could impact events with more planes involved since they appear to be the most common cause of a hit (see figure 6.1, first bin) and might occur at the same time as a muon event and hence disturb the correct detection of some tracks.

In figure 6.4, the calculated angular distribution, based on the geometric considerations of the setup, is compared with the expected angular distribution of chapter 5.2. The comparison shows that the measured distribution is in agreement with the expected distribution. The high uncertainties of the detected distribution are caused by low event numbers in the respective bins. Hence, the distribution could be improved by more statistics. The angular ranges of the bins cannot be changed effortlessly since they depend on the telescope geometry.

**Tracking based analysis** To verify which events might originate from muons, hits of all sensors are matched and a straight track is fitted. Afterwards, the goodness of the fits, was analyzed with the $\chi^2$-test. Most $\chi^2_{\text{red}}$ ($\frac{\chi^2}{dof}$) values are found in the range of 10 to 100, while a few exceed 100 or even 1000. The high $\chi^2_{\text{red}}$ values indicate a significant underestimation of the uncertainties. By investigation of the fit quality in relation to $\chi^2_{\text{red}}$, it was found that fits with $\chi^2_{\text{red}} \leq 100$ describe the data well. Hence, tracks with higher $\chi^2_{\text{red}}$ are not considered for the analysis of the angular distribution. The most probable reason for the high $\chi^2_{\text{red}}$ values is that the sensors were still slightly misaligned after the alignment process (see section 6.2.2). The alignment of the detector layers was not done with the cosmic data of the conducted experiment, but with testbeam data acquired with the same ALPIDE telescope. Considering the transport of the telescope to the testbeam location and back, the chips might have slightly moved and hence the alignment with the testbeam data does not reflect the sensor positions in the conducted experiment perfectly. As a consequence, the deviations in alignment from the true position lead to a systematic error, which cannot be quantified. This is one possibility to explain the underestimation of the errors and hence higher values of $\chi^2_{\text{red}}$.

Having the track classification done based on the $\chi^2_{\text{red}}$ distribution, more precise results are expected to be calculated in the second part of the analysis, in which the reconstructed muon tracks are used to determine the angular distribution. Here, a distinction is made between the angular distribution of 7-plane-events and the distributions of n-plane-events with $n < 7$. On the one hand, the distribution of 7-plane-events can be directly compared to the expected $cos^2(\theta)$-distribution. On the other hand, the distribution of n-plane-events with $n < 7$ do not reflect the true angular distribution of muons due to the geometrical constraints of the experimental setup. Hence, they can only be compared to a minimum and maximum zenith angle in which it is expected to detect the majority of the corresponding n-plane-events.

In figure 6.10 the angular distributions of n-plane-events are depicted. The distributions of events with $n < 7$ show a peak at different angles. A shift of the peaks to larger angles for events with less involved planes is observable. Moreover, the maximum zenith angles of the determined distributions are compared to the theoretical maximum angles and are shown in table 6.1. The measured angles $\Theta_n$ agree well with the expected angles $\theta''_n$ for the original detector geometry. The slight overestimation can be explained by the low probability of such events and the rather small statistics.

The expected angular distribution can be directly compared to the distribution of measured 7-plane-events shown in figure 6.9b, within the limits of a certain angular range. The measurable angular range of the 7-plane-events is narrow[1] due to the elongated placement of the detector layers. In this range, the detectable angular distribution agrees well with the expected $cos^2(\theta)$-distribution, except for the first and second bin. While the first bin is significantly lower, the second bin is higher than expected.

One possible reason for this low number is that one detector layer has a considerable inefficiency. This would lead to a high amount of 6-plane events. As shown in figure 6.10, this is not the case, as the majority of good tracks ($\chi^2_{\text{red}} \leq 100$) in the angular range of 0° to 2° are 7-plane-events. Therefore it is unlikely that the low number of events in the first bin is caused by inefficiency.

The most plausible reason for the low event number in the first bin and the high event number in the second bin is the non-optimal alignment of the detector, which was done with testbeam data. It influences the relative positions of the detector layers in the analysis and hence directly influences the zenith angle (see equation 6.5). Therefore, the misalignment might cause events with an angle of 0° to 2° to be measured with a systematically larger angle. If this is the case, the misaligned events will not be found in the first bin, but should appear in the second. This is in agreement with the observations since a significantly higher event number than expected, is observed in the second bin. Furthermore, the high amount of events that do not pass the $\chi^2_{\text{red}}$-cut in the second bin (see figure 6.9b) might indicate that minimal angle events are misaligned to the degree that they are not recognized as a straight track anymore and are determined as a bad track with a larger angle. This could be the case, especially for very small angles, since the misalignment has a greater impact on the fit quality if the projected track is short.

However, to confirm this suspicion, new measurements are needed. In these measurements, the dataset used for the alignment would need to be acquired in the same location and at the same time as the experiment to provide a correct align-

---

[1] The maximum possible detectable zenith angle of a 7-plane-event is calculated to approximately 15°. Detections at this angle are rather unlikely due to the rectangular shape of the detector. The detected distribution can be compared to the expected one, up to an angle of 11.3° (see A.2).

ment. The alignment data could be acquired with a collimated radioactive source, strong enough to penetrate the telescope. Another possible way to achieve a good alignment could be a long-term measurement with two scintillators as an external trigger, which would exclude events not originating from charged particles and provide the needed statistics for alignment. As a result, the data acquisition would be significantly more efficient and could be done over multiple weeks or months without any interruptions. This would provide good amount of events, which are suited for the alignment process with *Corryvreckan* [28]. Furthermore, *Corryvreckan* could be used for a full analysis of the data, also opening the possibility to get direct access to sensor performance parameters, e.g., efficiency, cluster size, and cluster shape.

Besides a correct alignment procedure, other improvements to the experiment can be explored. For instance, the geometrical constraints can be reduced with a tighter spacing of the detector layers in the telescope. This would result in larger angular acceptance for all n-plane-events, which would, in turn, improve the measurement of the angular distribution, in particular for larger angles. The currently used telescope is constructed for the use in testbeams, where a wider spacing of the detector layers is beneficial for the quality of the track reconstruction. Another source of errors, which could be eliminated, is the inconsistent threshold calibration for each layer. As shown in table 4.1, the thresholds of the detector layers vary significantly from one to another. Even if no direct impact on the data quality is found in the present analysis, it is preferable to have a comparable threshold calibration.

With these improvements of the experimental setup, a more detailed analysis of the detectable angular distribution of cosmic muons would be achievable.

**Summary** In this thesis, the ability of the ALPIDE sensors to detect cosmic muons and measure their angular distribution is investigated. According to the number of detected n-plane-events, the proper functioning of the detectors is verified. With the current experimental setup, a measurement of the angular distribution is achieved. In the range of more than 4°, it is in good agreement with the expected angular distribution of cosmic muons. However, smaller angles deviate from the expected angular distribution.

Small imperfections were identified in the experimental setup, which might have caused the deviations in the measurement of the angular distribution. With respect to the unfavorable adjustment of the setup, the obtained results are already remarkable. Therefore, a readjustment of the experiment could yield a precise confirmation of the expected angular distribution.

Furthermore, a continuation of this experiment might lead to more opportunities in the analysis, as an investigation of the efficiency by a more efficient track reconstruction. Moreover, a study of the cluster size and cluster shape[2] dependence on the inclination of an incident particle could be possible.

---

[2] A first investigation of the cluster size and shape that occurred in the acquired data is performed in [33].

# Appendices

# Appendix A

## A.1 Calculation of the muon energy loss traversing the ALPIDE telescope

To calculate the energy loss of cosmic muons, traversing the ALPIDE telescope, all materials have to be taken into account until the last sensor layer. The first material layer of the telescope, which has to be considered, is the beam entrance window. It consists of an aluminum foil (16 µm) and a polyimide film (kapton, $\sim 50$ µm), which shields the detectors from light. Inside the telescope case, there are seven ALPIDE sensors, which consist of a 50 µm thick silicon layer (see section 3.2). The significantly thinner metal layer on top of the silicon, providing the in-pixel circuitry, can be neglected in the following calculation. The detector layers are separated from each other and the beam entrance window by $\sim 2$ cm of air.

| Material | Density | Thickness | Energy loss for muons with | |
|---|---|---|---|---|
| | [g cm$^{-3}$] | [µm] | 1 GeV [keV] | 100 GeV [keV] |
| Kapton | 1.420 | 50 | 13.7 | 18.2 |
| Aluminum | 2.699 | 16 | 7.5 | 10.2 |
| Silicon | 2.329 | 50 | 21.0 | 28.5 |
| Air[1] | $1.205 \times 10^{-3}$ | $20 \times 10^{3}$ | 4.9 | 7.3 |

Table A.1: Mean energy loss by ionization of muons traversing components of the ALPIDE telescope. Material densities are taken from [35].

Table A.1 shows the energy loss of muons with different kinetic energies, traversing each medium. The energy loss is calculated with the Bethe-Bloch formula (see equation 2.3). A more precise calculation is achievable with the Landau model, as all dense materials are very thin. As shown for silicon in figure 2.5b, a calculation with the Bethe-Bloch formula leads to an overestimation of the energy loss of

---

[1] (dry, 1 atm [34])

around 100% for high kinetic energies. However, to calculate an estimate of the energy loss, it is sufficient to use the Bethe-Bloch formula, as long as the energy loss is neglectable small.
As shown in table A.1, the energy loss ranges from around 5 keV to 30 keV per traversed layer, which is negligible compared to the kinetic energy of the muon. Hence, the kinetic energy of the muon remains nearly constant. The energy loss through the entire telescope can be estimated by multiplying the energy loss by the number of layers of the related material.
The setup consists of seven layers of air and silicon, and one layer of kapton and aluminum, respectively. Hence, the energy loss for muons ranges from 200 keV to 280 keV for muons in the energy range 1 GeV to 100 GeV, which is still negligible compared to the muon energy.

## A.2 Maximum possible zenith angle of muons traversing the entire ALPIDE telescope

An incident muon, which traverses the entire ALPIDE telescope at the maximum possible zenith angle (considering the calculations made in section 5.1.2), has to traverse the first detector layer at the edge of the plane and the last layer at the edge on the opposite side. This trajectory is illustrated in figure 5.1b by $\theta_2$ in the case of two traversed detector layers. Thereby, the calculation of the maximum angle for seven detector layers is equal to the calculation for two layers. With simple geometric considerations, the angle can be calculated by

$$\begin{aligned} \theta &= \arctan\left(\frac{2 \cdot r_{\text{detector}}}{s_{\text{telescope}}}\right) && \text{(A.1)} \\ &= 11.3^\circ && \text{(A.2)} \end{aligned}$$

Here, $r_{\text{detector}} \simeq 1.2\,\text{cm}$ represents the detector radius and $s_{\text{telescope}} = 12\,\text{cm}$ the distance of the two outermost detector layers of the telescope.

In reality, muons can traverse the entire telescope at even higher angles. To calculate the true maximum angle, the original detector geometry has to be considered. In the original rectangular detector geometry the maximum zenith angle can be achieved, if a muon traverses, e.g., the top-left edge on the first plane and the bottom-right edge on the last plane. As a result, the true maximum angle can be calculated by

$$\theta = \arctan\left(\frac{\sqrt{x^2_{\text{detector}} + y^2_{\text{detector}}}}{s_{\text{telescope}}}\right) \tag{A.3}$$

$$= 15.6^\circ \tag{A.4}$$

Here $x_{\text{detector}}$ and $y_{\text{detector}}$ represent the detector dimensions of 1.5 cm × 3 cm. In reality, a particle traversing all seven detector planes would only rarely approach this large angle.

## A.3 Additional figure to the analysis

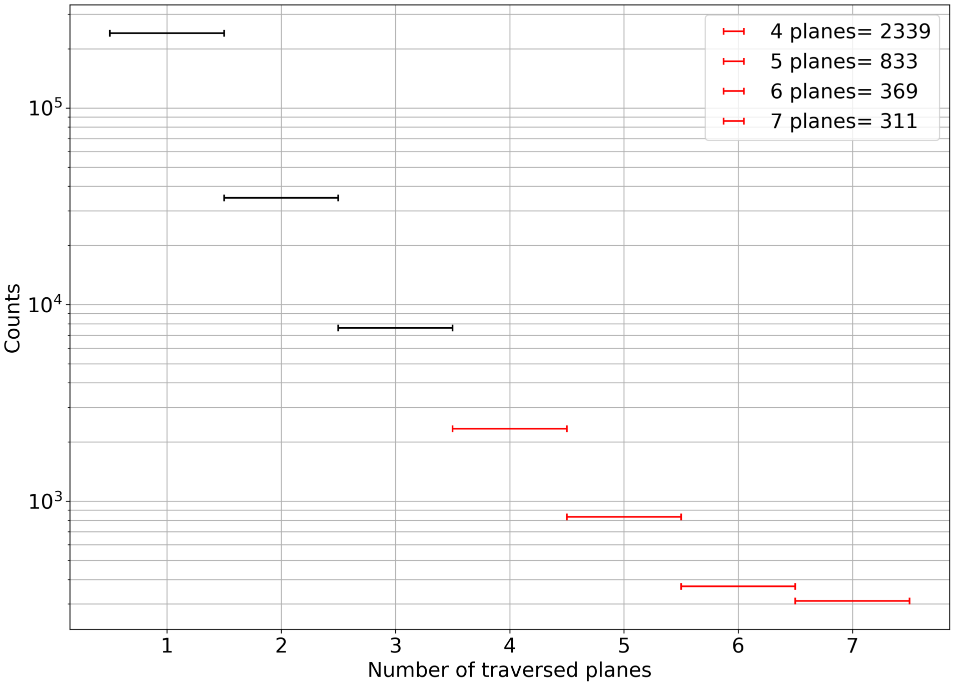

Figure A.1: Total number of measured n-plane-events.

# Bibliography

[1] *CERN homepage-History*. 2012. URL: `https://home.cern/about/who-we-are/our-history` (cited on page 1).

[2] *CERN homepage-The LHC*. 2012. URL: `https://home.cern/science/accelerators/large-hadron-collider` (cited on page 1).

[3] Kyrre Skjerdal. "Photoproduction of $\rho^0$ in ultra–peripheral nuclear collisions at ALICE". In: *J. Phys. : Conf. Ser.* 455.arXiv:1304.6850 (2013). URL: `https://cds.cern.ch/record/1544220` (cited on page 2).

[4] B Abelev et al. "The ALICE experiment at the CERN LHC. A Large Ion Collider Experiment". In: *JINST* (2008). Also published by CERN Geneva in 2010. DOI: `10.1088/1748-0221/3/08/S08002`. URL: `http://cds.cern.ch/record/1129812` (cited on pages 2, 3, 6).

[5] B Abelev et al. *Upgrade of the ALICE Experiment: Letter of Intent*. Tech. rep. CERN-LHCC-2012-012. LHCC-I-022. ALICE-UG-002. 2012. DOI: `10.1088/0954-3899/41/8/087001`. URL: `http://cds.cern.ch/record/1475243` (cited on page 3).

[6] K Aamodt et al. *Technical Design Report for the Upgrade of the ALICE Inner Tracking System*. Tech. rep. CERN-LHCC-2013-024. ALICE-TDR-017. 2013. DOI: `10.1088/0954-3899/41/8/087002`. URL: `http://cds.cern.ch/record/1625842` (cited on pages 4, 6, 21, 22, 29).

[7] James Philip Iddon. "Commissioning of the new ALICE Inner Tracking System". In: *JINST* arXiv:2005.01443. 08 (2020). DOI: `10.1088/1748-0221/15/08/C08009`. URL: `https://cds.cern.ch/record/2717344` (cited on page 5).

[8] W. Poonsawat et al. *Material Budget Calculation of the new Inner Tracking System, ALICE.* Tech. rep. arXiv:1706.02110. 13 pages, 9 figures, regular paper. 2017. URL: `https://cds.cern.ch/record/2274214` (cited on page 6).

[9] M. Thomson. *Modern Particle Physics*. Cambridge University Press, 2013 (cited on pages 7, 8).

[10] Wikimedia Commons. *Standard model of elementary particles*. [Online; accessed Oct. 31, 2020]. URL: `https://commons.wikimedia.org/wiki/File:Standard_Model_of_Elementary_Particles.svg` (cited on page 8).

[11] *Cosmic Rays (PDG)*. 2011. URL: `https://pdg.lbl.gov/2011/reviews/rpp2011-rev-cosmic-rays.pdf` (cited on pages 8–11, 34).

[12] *PDG-muon list*. 2020. URL: `https://pdg.lbl.gov/2020/listings/rpp2020-list-muon.pdf` (cited on page 10).

[13] P.K.F. Grieder. *Cosmic rays at earth: researcher's reference manual and data book*. ELSEVIER SCINECE B.V., 2001, pp. 356–358,403. URL: `http://theor.jinr.ru/~vnaumov/Eng/JINR_Lectures/books/Grieder2001.pdf` (cited on pages 10, 36).

[14] S. Cecchini and M. Spurio. "Atmospheric muons: experimental aspects". In: arXiv:1208.1171 (2012). URL: `https://arxiv.org/pdf/1208.1171.pdf` (cited on page 10).

[15] *Muon stopping power and range tables, 10 MeV-100 TeV (PDG)*. 2020. URL: `https://pdg.lbl.gov/2020/AtomicNuclearProperties/adndt.pdf` (cited on pages 11–13, 35).

[16] C. Grupen. "Physics of Particle Detection". In: arXiv:9906063 (1999). URL: `https://arxiv.org/pdf/physics/9906063v1.pdf` (cited on page 12).

[17] W. R. Leo. *Techniques for Nuclear and Particle Physics Experiments*. Springer-Verlag Berlin Heidelberg GmbH, 1994 (cited on pages 14–19).

[18] Wikimedia Commons. *Band gap comparison*. [Online; accessed Nov. 16, 2020; changes are made]. URL: `https://commons.wikimedia.org/wiki/File:Band_gap_comparison.svg?uselang=de` (cited on page 14).

[19] Wikimedia Commons. *Covalent bonding in silicon*. [Online; accessed Nov. 16, 2020]. URL: `https://commons.wikimedia.org/wiki/File:Covalent_bonding_in_silicon.svg` (cited on page 14).

[20] M. Suljic. "Study of Monolithic Active Pixel Sensors for the Upgrade of the ALICE Inner Tracking System". In: (2017). URL: `http://cds.cern.ch/record/2303618` (cited on pages 15, 20–22, 26, 27).

[21] Wikimedia Commons. *pn-junction equilibrium graph*. [Online; accessed Nov. 21, 2020]. URL: `https://commons.wikimedia.org/wiki/File:Pn-junction-equilibrium-graph.svg` (cited on page 18).

[22] L. Rossi et al. *Pixel Detectors: From Fundamentals to Applications*. Springer-Verlag, 2005 (cited on pages 20, 51).

[23] M. Mager. "ALPIDE, the Monolithic Active Pixel Sensor for the ALICE ITS upgrade". In: (2016). URL: `https://doi.org/10.1016/j.nima.2015.09.057` (cited on pages 22, 36).

[24] A. Bessona, A. Perez Perez, and E. Spiritic. "From vertex detectors to inner trackers with CMOS pixel sensors". In: (2016). URL: `http://cds.cern.ch/record/2145663/files/arXiv:1604.02957.pdf` (cited on page 22).

[25] ALICE ITS ALPIDE development team. *ALPIDE Operations Manual*. 2016 (cited on pages 23–26).

[26] M. Keil and F. Reidt. *ALPIDE Software - User manual*. 2018 (cited on page 28).

[27] *Protocol of muon measurements with the ALPIDE telescope*. 2020. URL: `https://1drv.ms/x/s!ApBKVWM_10sYz0_JnPJ-EI0i3MM6?e=0teYrr` (cited on page 32).

[28] D. Dannheim et al. *Corryvreckan: A Modular 4D Track Reconstruction and Analysis Software for Test Beam Data*. Tech. rep. Centrum voor Wiskunde en Informatica (CWI), 1995. URL: `https://arxiv.org/abs/2011.12730` (cited on pages 32, 51, 52, 63).

[29] G. van Rossum. *Python tutorial*. Tech. rep. Centrum voor Wiskunde en Informatica (CWI), 1995 (cited on pages 33, 46).

[30] *Muons in shielding concrete (PDG)*. 2020. URL: `https://pdg.lbl.gov/2020/AtomicNuclearProperties/MUE/muE_shielding_concrete.pdf` (cited on page 35).

[31] Andy Anderson. *A sphere with two solid angles subtending one steradian each in different directions.* [Online; accessed Oct. 14, 2020]. URL: `https://commons.wikimedia.org/wiki/File:Solid_Angle,_1_Steradian.svg` (cited on page 38).

[32] D. Donner. "B.Sc. thesis–In preparation". In: (2021) (cited on page 53).

[33] F. Franke. "B.Sc. thesis–In preparation". In: (2021) (cited on page 64).

[34] *Gas densities and optical properties*. 2020. URL: `https://pdg.lbl.gov/2020/AtomicNuclearProperties/explain_gas.html` (cited on page 66).

[35] *Atomic and Nuclear Properties of Materials for more than 350 materials*. 2020. URL: `https://pdg.lbl.gov/2020/AtomicNuclearProperties/` (cited on page 66).

# Acknowledgment

First and foremost, I would like to express my deepest gratitude to Silvia Masciocchi, who gave me the opportunity to join the ALICE group at GSI and to perform the measurements for this thesis with an ALPIDE telescope. I am grateful for her dedicated and enthusiastic nature, which motivated me a lot. In particular, I would like to thank her for the opportunity to participate in the testbeam at DESY, which was an extraordinary experience that made a dream come true for me.

Moreover, I would like to thank Klaus Reygers for kindly accepting to be the second referee for my thesis.

Furthermore, I would like to thank Bogdan Blidaru for his humor, kind supervision, and helpful comments and ideas concerning this thesis. Especially in the final phase of the thesis, I could always count on him, although he had a huge workload himself.

Likewise, Pascal Becht deserves my greatest appreciation for his helpful advice and comments concerning my thesis.

In addition to that, I want to thank Bogdan, Pascal, and Maurice for the unforgettable experiences we shared during the testbeam. Despite the lack of sleep and the problems we had to face, it was an incredible time.

I am indebted to Marius and Carolina for supporting me and improving this thesis with their engaged proofreading of many chapters.

Furthermore, I want to express my deepest gratitude from the bottom of my heart to Justyna, who supported me by proofreading and also in any way she could whenever I needed her.

In general, I want to show my gratitude to all people who are not mentioned by name but supported me during my whole studies.

Наконец, я хотел бы от всего сердца поблагодарить свою семью за их любовь, помощь и поддержку. Без них я бы не был тем, кто я являюсь сегодня.

# Declaration

I declare that this thesis has been composed solely by myself and that it has not been submitted, in whole or in part, in any previous application for a degree. Except where states otherwise by reference or acknowledgment, the work presented is entirely my own.

Heidelberg, February 8, 2021

David Schledewitz